Cell Reports

Article

Aldehydes alter TGF-β signaling and induce obesity and cancer

Graphical abstract

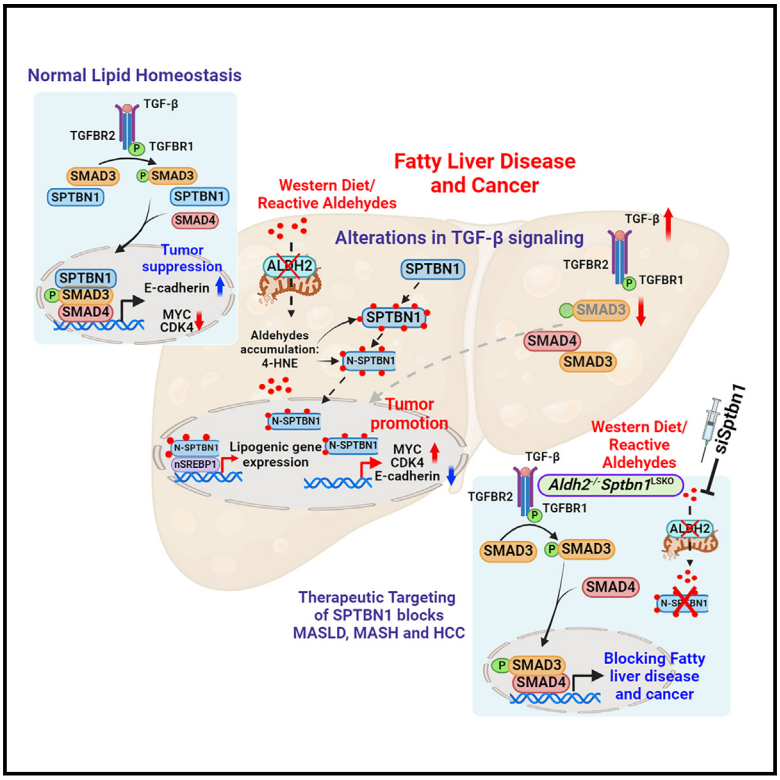

Highlights

- ALDH2 and SPTBN1 alterations lead to obesity, MASH, and HCC
- Disruption of TGF-β signaling by toxic cleavage of Smad3 adaptor SPTBN1
- SPTBN1 is a potential therapeutic target for MASH and HCC

Authors

Xiaochun Yang, Krishanu Bhowmick, Shuyun Rao, ..., Hai Huang, Adrian R. Krainer, Lopa Mishra

Correspondence

lopamishra2@gmail.com

In brief

Yang et al. reveal how accumulated endogenous toxins—aldehydes—produced by a Western diet disrupts TGF-β signaling, leading to MASLD/MASH and cancer. Targeting SPTBN1 (SMAD3 adaptor) blocks aldehyde-induced SPTBN1 cleavage and adduct formation, offering a non-toxic approach to achieving beneficial responses in patients with MetS, MASH, and cancer.

Yang et al., 2024, Cell Reports *43*, 114676
September 24, 2024
https://doi.org/10.1016/j.celrep.2024.114676

CellPress

Cell Reports

CellPress
OPEN ACCESS

Article

Aldehydes alter TGF-β signaling and induce obesity and cancer

Xiaochun Yang,[1,2,15] Krishanu Bhowmick,[1,2,15] Shuyun Rao,[3,15] Xiyan Xiang,[1,2] Kazufumi Ohshiro,[1] Richard L. Amdur,[4] Md. Imtaiyaz Hassan,[5] Taj Mohammad,[5] Keith Crandall,[6] Paolo Cifani,[2] Kirti Shetty,[7] Scott K. Lyons,[2] Joseph R. Merrill,[2] Anil K. Vegesna,[1,2] Sahara John,[1,2] Patricia S. Latham,[8] James M. Crawford,[9] Bibhuti Mishra,[1,10] Srinivasan Dasarathy,[11] Xin Wei Wang,[12] Herbert Yu,[13] Zhanwei Wang,[13] Hai Huang,[14] Adrian R. Krainer,[2] and Lopa Mishra[1,2,3,16,*]

[1]Institute for Bioelectronic Medicine, Divisions of Gastroenterology and Hepatology, Department of Medicine, Feinstein Institutes for Medical Research, Northwell Health, Manhasset, NY 11030, USA

[2]Cold Spring Harbor Laboratory, Cold Spring Harbor, NY 11724, USA

[3]Department of Surgery, George Washington University, Washington, DC 20037, USA

[4]Quantitative Intelligence Unit, The Institutes for Health Systems Science & Bioelectronic Medicine, Feinstein Institutes for Medical Research, Northwell Health, Manhasset, NY 11030, USA

[5]Centre for Interdisciplinary Research in Basic Sciences, Jamia Millia Islamia, Jamia Nagar, New Delhi 110025, India

[6]Computational Biology Institute, Department of Biostatistics and Bioinformatics, George Washington University, Washington, DC 20037, USA

[7]Department of Gastroenterology and Hepatology, the University of Maryland, School of Medicine, Baltimore, MD 21201, USA

[8]Department of Pathology, George Washington University, Washington, DC 20037, USA

[9]Department of Pathology and Laboratory Medicine, Donald and Barbara Zucker School of Medicine at Hofstra, Northwell Health, Manhasset, NY 11030, USA

[10]Department of Neurology, Northwell Health, Manhasset, NY 11030, USA

[11]Division of Gastroenterology and Hepatology, Cleveland Clinic, Cleveland, OH 44106, USA

[12]Laboratory of Human Carcinogenesis, Liver Cancer Program, Center for Cancer Research, National Cancer Institute, Bethesda, MD 20892, USA

[13]Epidemiology Program, University of Hawaii Cancer Center, Honolulu, HI 96813, USA

[14]Center for Immunology and Inflammation, Feinstein Institutes for Medical Research, Donald and Barbara Zucker School of Medicine at Hofstra, Northwell Health, Manhasset, NY 11030, USA

[15]These authors contributed equally

[16]Lead contact

*Correspondence: lopamishra2@gmail.com

https://doi.org/10.1016/j.celrep.2024.114676

SUMMARY

Obesity and fatty liver diseases—metabolic dysfunction-associated steatotic liver disease (MASLD) and metabolic dysfunction-associated steatohepatitis (MASH)—affect over one-third of the global population and are exacerbated in individuals with reduced functional aldehyde dehydrogenase 2 (ALDH2), observed in approximately 560 million people. Current treatment to prevent disease progression to cancer remains inadequate, requiring innovative approaches. We observe that *Aldh2*$^{-/-}$ and *Aldh2*$^{-/-}$*Sptbn1*$^{+/-}$ mice develop phenotypes of human metabolic syndrome (MetS) and MASH with accumulation of endogenous aldehydes such as 4-hydroxynonenal (4-HNE). Mechanistic studies demonstrate aberrant transforming growth factor β (TGF-β) signaling through 4-HNE modification of the SMAD3 adaptor SPTBN1 (β2-spectrin) to pro-fibrotic and pro-oncogenic phenotypes, which is restored to normal SMAD3 signaling by targeting *SPTBN1* with small interfering RNA (siRNA). Significantly, therapeutic inhibition of SPTBN1 blocks MASH and fibrosis in a human model and, additionally, improves glucose handling in *Aldh2*$^{-/-}$ and *Aldh2*$^{-/-}$*Sptbn1*$^{+/-}$ mice. This study identifies SPTBN1 as a critical regulator of the functional phenotype of toxic aldehyde-induced MASH and a potential therapeutic target.

INTRODUCTION

Identifying non-toxic targets for the treatment of metabolic disorders may enable the development of therapies that selectively blunt the harmful effects of high-fat diets, excessive alcohol consumption, or impaired metabolism of reactive aldehydes.[1] This is particularly challenging for drug development where short half-life, lack of tissue specificity, and immunogenicity limit enzyme-based therapies.[2] Endogenously produced reactive aldehydes are linked to the development of multiple diseases, including diabetes, insulin resistance, dyslipidemia, metabolic dysfunction-associated steatohepatitis (MASH), and atherosclerosis.[3–7]

These diseases are also associated with metabolic syndrome (MetS), which is characterized by abdominal obesity, hyperglycemia, hypertriglyceridemia, and hypertension. Globally, MetS affects approximately 25% of all adults.[8] As key regulators of physiological metabolism, fat tissue and the liver are particularly important in MetS.[9,10] The frequencies of obesity-associated metabolic dysfunction-associated steatotic liver disease (MASLD) and MASH are increasing alarmingly throughout the world, and these diseases contribute to increased risk of not only MetS but also hepatocellular carcinoma (HCC).[11] While multiple molecular pathways have been implicated in MetS, how crucial signaling pathways involved in MetS, liver disease, and fibrosis are linked to reactive aldehyde injury remains largely undefined.[7,12,13]

Aldehyde dehydrogenase 2 (ALDH2) is an NAD(P^+)-dependent mitochondrial enzyme critical for metabolizing highly reactive endogenous and exogenous aldehydes.[3] A mutant allele of *ALDH2* (rs671, G>A), referred to as *ALDH2*2*, is carried by ~560 million people. This dominant-negative mutation destabilizes the tetrameric enzyme, diminishing ALDH2 function, converting acetaldehyde to acetate, and interfering with alcohol metabolism.[14–16] Besides alcohol-related diseases, the *ALDH2* mutation is associated with MetS, HCC, and gastrointestinal cancers.[3,17–19] Compared to wild-type (WT) mice, homozygous *Aldh2* knockout mice exhibit increased susceptibility to toxicities caused by alcohol ingestion or aldehyde inhalation and altered immune-mediated metabolism.[20] On a high-fat diet, male heterozygous (*Aldh2*1/*2*) and homozygous (*Aldh2*2/*2*) knockin mice exacerbated MASLD progression and MetS.[21] Seo et al. reported *Aldh2*-deficient (global knockout *Aldh2*$^{-/-}$, *Aldh2*1/*2* mutant, and *Aldh2* liver-specific knockout) mice are more susceptible to CCl4 plus alcohol-associated liver fibrosis and HCC development.[22] Replacement or activation of ALDH2 has proven problematic despite identifying small-molecule activators, but it has not yet been taken to clinical trials.[21,23]

Transforming growth factor β (TGF-β) signaling plays a significant yet complex role in regulating energy homeostasis and chronic liver conditions, from simple steatosis to severe MASH.[24–28] Recent studies indicate decreased expression levels of genes in the TGF-β signaling pathway in overweight and obese adults.[25] High TGF-β1 levels are associated with human adiposity.[26] Moreover, *Smad3* loss or TGF-β receptor II loss protects from diet-induced obesity, insulin resistance, and hepatic steatosis.[24,26–28] TGF-β drives fibrosis and cancer through aberrant SMAD2/3 activation by TGF-β receptor1/2 and initiates the expression of extracellular matrix components by directly targeting PAI-1, CTGF, c-Jun, CDK4, and others.[29–31] Moreover, while multiple studies targeting TGF-β signaling through antibodies,[32] targeting TGF-β receptor1/2 by small-molecule inhibitors, have demonstrated alleviation of fibrosis and tumor progression, clinical benefits have remained elusive because of challenges that include off-target toxicities among other issues.[33–35]

SPTBN1 (also called β2-spectrin or β2SP) is a SMAD3 adaptor protein with functions in the cytoplasm and nucleus.[36] Through its interactions with SMAD3, SPTBN1 influences transcriptional-regulated targets of TGF-β, important for genomic stability, WNT signaling, and tumorigenesis.[37–41] Mice heterozygous for *Sptbn1* (*Sptbn1*$^{+/-}$), alone or when combined with the heterozygosity of *Smad3* (*Smad3*$^{+/-}$*Sptbn1*$^{+/-}$) spontaneously develop severe fatty liver disease, fibrosis, inflammation, and cancers. These data suggest that gene dosage of *Smad3* or *Smad3* and *Sptbn1* drives disease and tumorigenesis. With nearly 40% of human liver and gastrointestinal cancers having genetic alterations in TGF-β pathway components—mutations being predominantly heterozygous—these haploid mouse mutant models represent physiologically relevant systems for studying liver disease and cancer and understanding the "gene dosage" effect of TGF-β pathway members.[42,43]

Structurally, SPTBN1 is composed of a spectrin repeat section flanked by a pair of calponin-homology domains at the N terminus and a pleckstrin-homology domain at the C terminus. A caspase-3 cleavage site (^{1454}DEVD^{1457}) is present in the spectrin repeat 11. In stressed cultured hepatocytes, caspase-3 activity is induced and cleaves SPTBN1 into N-terminal and C-terminal products.[44] These caspase-cleaved SPTBN1 fragments also contribute to acetaminophen-induced liver damage.[44] SPTBN1 has a liver-specific role in response to diet-induced fatty liver, where caspase cleavage leads to spectrin fragments that interact with the lipogenic transcription factor SREBP1 and promote SREBP1-driven *de novo* lipogenesis.[45] The expression of genes involved in either fatty acid metabolism or *de novo* lipogenesis, such as *CIDEC*, *FASN*, *SCD1*, and *ACC1,* which SREBP1c induces, were highly activated by the cleaved spectrin-SREBP1c complex.[45] Several studies indicate a potential connection between spectrin and alcohol-related liver disease or liver disease associated with ALDH2 deficiency.[37] Homozygous *Sptbn1* knockout (*Sptbn1*$^{-/-}$) is embryonic lethal in mice, and *Sptbn1*$^{-/-}$ mouse embryos exhibit a phenotype resembling fetal alcohol syndrome and are highly susceptible to alcohol-induced death.[37,38,41] Adult *Sptbn1*$^{+/-}$ mice develop progressive liver disease and HCC and have increased levels of *Aldh2* and malondialdehyde in the liver when given alcohol.[37] Blockade of liver-specific βII-spectrin (*Sptbn1*^{LSKO}) is remedial, and it could be reflective of importance of inhibiting toxic effects of SPTBN1 fragments as well as dosage/abundance in TGF-β pathway members serving as potential rate-limiting steps in signaling for this pathway. Collectively, these findings suggest that SPTBN1 has a role in regulating enzymes involved in alcohol and aldehyde metabolism.

We evaluated cohorts of patients with high or low body mass index (BMI) and patients with either MASLD or MASH for differences in *SPTBN1* or *ALDH2* expression and for single-nucleotide polymorphisms (SNPs) in these genes. On the basis of those findings, our animal model studies above, the known effects of ALDH2 deficiency in humans, and the role of SPTBN1 in liver diseases, we crossed *Aldh2*$^{-/-}$ mice and *Sptbn1*$^{+/-}$ mice to explore the impact on MetS/MASLD/cancer development. Surprisingly, *Aldh2*$^{-/-}$ and *Aldh2*$^{-/-}$*Sptbn1*$^{+/-}$ (we refer to the latter as ASKO) mice spontaneously develop characteristics of MetS and MASLD or the more severe fibrotic condition MASH on a normal chow diet. Transcriptomic, metabolomic, and lipidomic analyses identified dramatic changes in liver metabolism, including increased amounts of 4-hydroxynonenal (4-HNE), in these mutant mice. We identified that abnormal accumulation of reactive aldehydes aberrantly adducted with cleaved

SPTBN1 fragments alters normal TGF-β signaling, promoting injury and lipogenesis that ultimately manifests in MetS and cancer. Strikingly, when we targeted *Sptbn1*, both small interfering RNA (siRNA)-mediated knockdown and genetic liver-specific knockout blocked interactions between reactive aldehydes and SPTBN1, significantly inhibiting MASH fibrosis, lipid accumulation, tissue damage, and cancer in the liver. Thus, SPTBN1 may represent a non-enzymatic target for treating MetS, MASH, and HCC.

RESULTS

Polymorphisms in human *SPTBN1* and *ALDH2* are associated with human obesity and fatty liver diseases

Genetic variants in *ALDH2* alter ALDH2 function and contribute to MASH and alcohol sensitivity.[14,16] A prominent point mutation in *SPTBN1* is associated with HCC.[46] Therefore, we evaluated for differences in *SPTBN1* or *ALDH2* expression levels in individuals with steatosis or MASH or those who were obese but otherwise healthy. Patients with MASH, obesity, type 2 diabetes, and type 2 diabetes with HCC had higher levels of liver SPTBN1 (Figures 1A, 1B, and S1A–S1C; $p < 0.05$). *ALDH2* mRNA abundance was not significantly different among these comparisons, although we note a greater variation among MASH patients (Figures 1A, 1B, S1A, and S1B).

Next, we explored *ALDH2* and *SPTBN1* loci for SNPs significantly associated ($p < 0.001$) with obesity, defined as BMI $\geq$30 (Table S1), or in patients with fatty liver diseases, including both MASLD and MASH (Table S2). Among the 3,115 individuals, we identified a total of 52 SNPs in these loci, including seven in the *ALDH2* locus and 45 in the *SPTBN1* locus, and 22 of them reached the significance threshold of 0.05 (Table S3). We evaluated the frequency of SNPs in 613 individuals with a BMI $\geq$30 compared with 558 with a normal weight (BMI <25) (Table S1). We identified a single SNP in the *ALDH2* locus (rs968529) and a single SNP in the *SPTBN1* locus (rs2941583) with significant associations (adjusted *p* value of 0.00096154 [0.05/52]) (Figure S1D; $p < 0.001$) (Table S3).

To assess the potential effects of these SNPs, we performed expression quantitative trait loci analyses using data from GTEx (genotype-tissue expression program). The result indicated that these variants could influence *ALDH2* or *SPTBN1* gene expression in a tissue-specific manner (Table S4). While SNPs reaching the $p < 0.001$ significance threshold were not identified in the 210 patients with fatty liver disease (Tables S2 and S3), using the non-adjusted *p* value of less than 0.05 two SNPs in the *SPTBN1* locus (rs7599241 and rs17046097) were associated with high BMI and fatty liver diseases (Figure S1E). The SNPs are present in intronic sequences of the *ALDH2* and *SPTBN1* genes and in genomic regions that encode multiple products.

Heterozygous loss of *Sptbn1* promotes development of MetS, MASLD, and MASH in mice with *Aldh2* deficiency on a normal diet

To explore the impact of *Sptbn1* deficiency on MetS and MASLD development in *Aldh2*-deficient mice, we intercrossed $Aldh2^{-/-}$ mice with $Sptbn1^{+/-}$ mice to generate $Aldh2^{-/-}Sptbn1^{+/-}$ (ASKO) mice. Genotypes of mice were confirmed by western blot (Figure S2A). ASKO mice were viable and fertile.

From 3 to 4 months of age, body weights of ASKO mice deviated from single mutant ($Aldh2^{-/-}$ or $Sptbn1^{+/-}$) and WT mice, and at 12 months by 29.2% (Figure 1C; $p < 0.05$). ASKO mice had significantly elevated visceral fat (epididymal white adipose tissue [eWAT]) accumulation (Figures 1D and S2B) on a normal chow (NC) diet. To gain deeper insights into body weight gain, we performed whole-body computed tomography (CT). We found that ASKO mice on the NC diet showed a trend toward a greater fat volume (31.57% ± 2.81% vs. 18.97% ± 2.93%) and less lean tissue volume (47.73% ± 1.45% vs. 56.13% ± 3.03%) than WT mice (Figures 1E and 1F). Moreover, we found that ASKO mice fed a Western diet (WD) showed a significant increase in fat volume (36.13% ± 2.02% vs. 16.6% ± 0.54%, $p < 0.05$) and decreased lean tissue volume (45.89% ± 1.71% vs. 57.8% ± 1.29%, $p < 0.05$) than WT mice fed WD (Figures S2C and S2D). These results suggest that increased adiposity is a key contributor to body weight. Increased adiposity is accompanied by abnormalities in glucose metabolism in ASKO mice. At 11 months of age, the serum glucose level of ASKO mice (289.4 ± 25.7 mg/dL) was 1.5-fold higher than that of WT mice (191.6 ± 7.8 mg/dL, $p < 0.05$) but not significantly different from those of single mutant mice ($Aldh2^{-/-}$ or $Sptbn1^{+/-}$) (Figure 1G). Glucose tolerance tests (GTTs) showed impaired glucose elimination in both $Aldh2^{-/-}$ and ASKO mice (Figure 1G). Accompanied with impaired glucose elimination, ASKO mice had significantly higher blood insulin concentrations than WT mice. Similarly, insulin tolerance tests (ITTs) indicated that ASKO mice displayed 24%–45% (Figure 1G; $p < 0.05$) higher blood glucose levels than those of WT and single mutant mice, suggesting increased insulin resistance in ASKO mice (Figure 1G). Further, we measured WAT lipolysis in WT, $Sptbn1^{+/-}$, $Aldh2^{-/-}$, and ASKO mice. We observed increased *ex vivo* lipolysis (fatty acids and glycerol release) in eWAT/inguinal WAT of ASKO mice compared to WT, $Sptbn1^{+/-}$, and $Aldh2^{-/-}$ mice (Figure S2E), suggesting that functional changes in eWAT may contribute to the development of MetS in ASKO mice. To understand the tissue specificity of insulin resistance, we analyzed *p*-Akt, a major node downstream of insulin signaling in liver, adipose, and muscle tissues. Our results showed decreased levels of *p*-Akt in the liver, adipose, and muscle tissues of ASKO mice, indicating that insulin resistance is not limited to the liver tissue only (Figure S2F). Interestingly, we observed ASKO mice develop a loss of muscle mass (sarcopenia) similar to that in patients with MASH. This is accompanied by elevated levels of myostatin, a TGF-β superfamily member expressed primarily in skeletal muscle, which inhibits muscle growth and causes sarcopenia in cirrhosis. These effects are mitigated in the liver-specific knockout of SPTBN1 ($Sptbn1^{LSKO}$). Conversely, myostatin expression is diminished in $Sptbn1^{LSKO}$ tissues, reflecting the complexities in tissue-specific effects.[47]

In addition, we found that ASKO mice had higher serum triglyceride (TG) levels ($p < 0.05$), liver weight ($p < 0.01$), and serum alanine transaminase (ALT) levels than those in WT and single mutant mice (Figure 1H), suggesting increased severity of liver damage in ASKO mice. Histology showed an abnormal liver architecture with possible ballooning, increased microvesicular

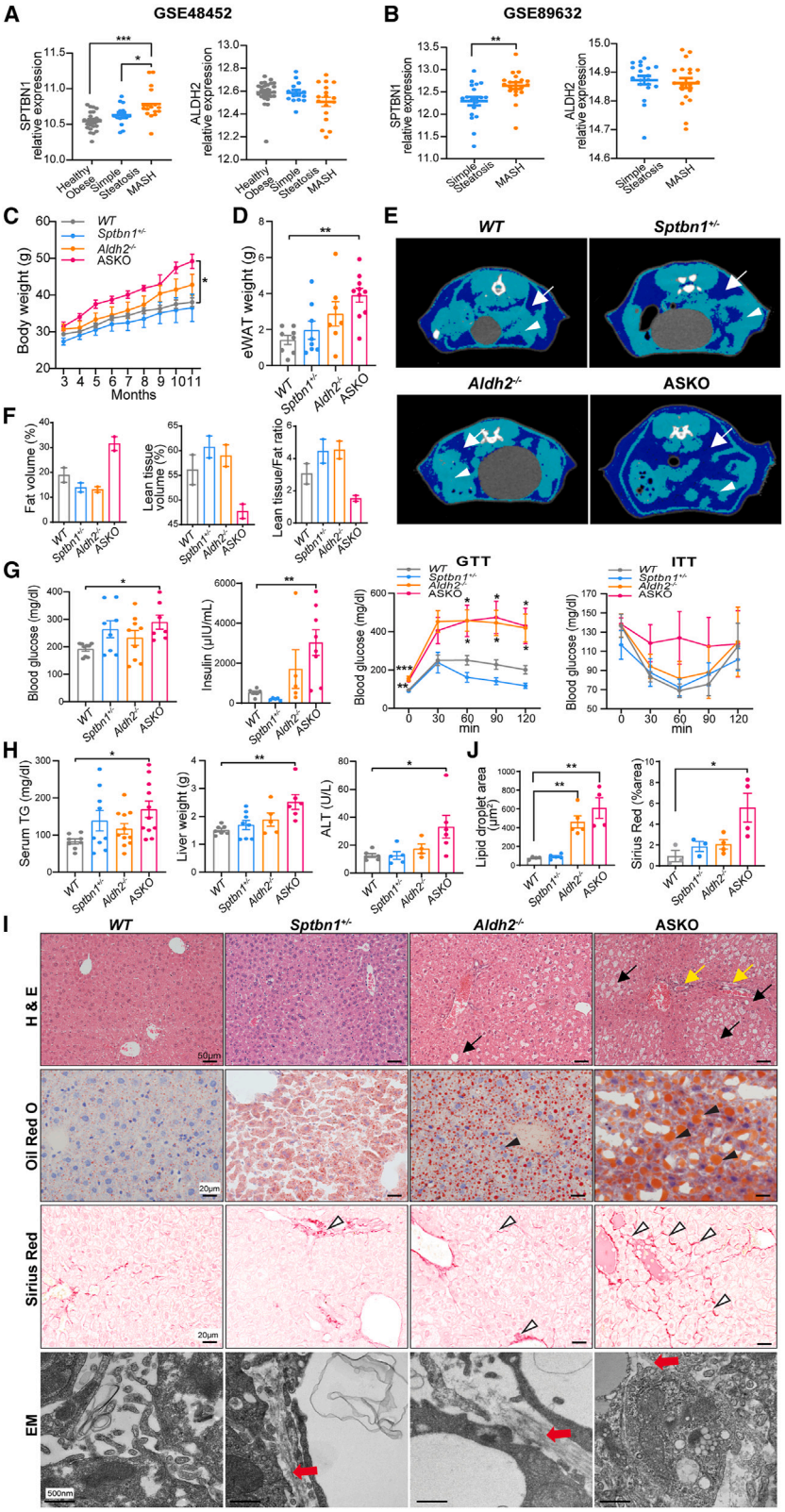

Figure 1. SPTBN1 alterations are associated with obesity and MASH in human patients, and ASKO (*Aldh2*$^{-/-}$*Sptbn1*$^{+/-}$) mice develop MetS, MASLD, and MASH on a normal diet

(A) Relative mRNA abundance of *SPTBN1* is increased compared to *ALDH2* in liver tissue samples from patients with MASH (n = 17) compared to liver tissue samples from healthy obese individuals (n = 25) or patients with simple steatosis (n = 14) from GSE48452. Data are presented as mean ± SEM. $^{*}p < 0.05$, $^{***}p < 0.001$.

(B) Relative mRNA abundance of *SPTBN1* is increased compared to *ALDH2* in liver tissue samples from patients with MASH (n = 19) compared to liver tissue samples from simple steatosis (n = 19) from GSE89632. Data are presented as mean ± SEM. $^{**}p < 0.01$.

(C) Body weight of the four genotypes was measured from 3 to 12 months of age. Statistically significant differences in body weight were determined by one-way ANOVA with Bonferroni's multiple comparisons test comparing the averaged body weight of each mutant over time to the WT (n = 4–9). Data are presented as mean ± SEM. $^{*}p < 0.05$.

(D) Epididymal white adipose (eWAT) tissue weight of the indicated mice genotypes at 44–48 weeks old. Data are presented as mean ± SEM. Significant differences in eWAT weight were determined by pairwise t tests (n = 7–10 mice/genotype). $^{**}p < 0.01$.

(E) Lean tissue volume and fat volume were measured by whole-body CT scan of each genotype on normal diet. Representative cross-sectional images (at L5) of each genotype are shown. Light blue (arrowheads) indicates lean tissue, and dark blue (arrows) indicates fat tissue.

(F) Graph showing the percentage of fat volume, lean tissue volume, and lean tissue/fat ratio (n = 2 mice/genotype). Data are presented as mean ± SEM.

(G) Basal blood glucose level, basal blood insulin level, and blood glucose levels during GTT and ITT of 44- to 48-week-old mice. Statistical differences in blood glucose (n = 7–9 mice/genotype) and insulin (n = 5–8 mice/genotype) levels were determined by pairwise t tests. Different values at each time point in GTT (n = 5–6 mice/genotype) and ITT (n = 3–5 mice/genotype) studies were determined by one-way ANOVA with Bonferroni's multiple comparisons test. Data are presented as mean ± SEM. $^{*}p < 0.05$, $^{**}p < 0.01$, $^{***}p < 0.001$.

(H) Serum TG levels (n = 8–11 mice/genotype), liver weight (n = 5–8 mice/genotype), and circulating ALT (n = 4–6 mice/genotype) levels in 44- to 48-week-old mice are presented as mean ± SEM. Pairwise t tests determined statistical differences. $^{*}p < 0.05$, $^{**}p < 0.01$.

(I) Representative histology images with hematoxylin and eosin (H&E) staining, Oil Red O staining, Sirius red staining, and electron microscopy (EM) images of the liver of 44-week-old WT, *Sptbn1*$^{+/-}$, *Aldh2*$^{-/-}$, and ASKO mice. H&E-stained images (top panels) show micro- and macrovesicular lipids (black arrows) and inflammation (yellow arrows). Second row: Oil Red O-stained images showing fat droplets (black arrowheads). Third row: Sirius red-stained images showing fibrosis (open arrowheads). Red

(legend continued on next page)

and macrovesicular lipid droplet accumulation within hepatocytes, and fibrosis in ASKO mice (Figures 1I and 1J). Collectively, these results indicated that ASKO mice spontaneously develop phenotypes resembling MetS and MASLD/MASH on NC diet compared to the single mutants and WT mice.

Transcriptional regulation of lipid metabolism is altered in the livers of *Aldh2*$^{-/-}$ and ASKO mice

To understand the mechanisms for the differences in liver metabolism in ASKO mice, we performed bioinformatics analysis of RNA-sequencing (RNA-seq) data using Ingenuity "Upstream Regulator" in Ingenuity Pathway Analysis (IPA). RNA-seq profiling uncovered that expression of genes associated with liver diseases was enriched in livers from ASKO mice compared to those from WT mice (Figure S3A). For IPA, we included only those regulators with *Z* scores of more than 2 or less than −2 when transcriptional profiles of livers from *Aldh2*$^{-/-}$ or ASKO mice were compared to those from WT mice (Figure S3B). We further evaluated expression of a selected set of genes involved in either fatty acid metabolism or *de novo* lipogenesis in the livers of mice of the four genotypes. For genes encoding proteins involved in fatty acid metabolism, *CIDEC* is induced by insulin, SREBP1c, and PPARγ, *G0S2* by PPARα, and *CD36* by PPARγ. For genes encoding proteins involved in *de novo* fatty acid synthesis, *FASN*, *SCD1*, and *ACC1* are induced by ChREBP, SREBP1c, and PPARγ.[48] Compared to the livers of WT mice, all six genes exhibited increased transcript abundance in the livers of ASKO mice (Figures S3C–S3F). Of the above, we confirmed upregulation of *CD36, G0S2,* and *CIDEC* by RT-PCR and single-nucleus RNA-seq (snRNA-seq) analysis (Figures S3G and S3H).

Metabolic changes in *Aldh2*$^{-/-}$ and ASKO mice on a normal diet

The results described above led us to characterize liver metabolism in these mice further. By comparing metabolites and lipids in the livers (Table 1), we found that the *Aldh2*$^{-/-}$ mice had altered activity of pathways associated with fatty acid metabolism and *de novo* fatty acid synthesis compared to WT mice. Consistent with the more complex phenotype of the ASKO mice than the *Aldh2*$^{-/-}$ mice, many more metabolic systems were affected in ASKO mice than in the *Aldh2*$^{-/-}$ mice, including those associated with amino acid metabolism, carbohydrate metabolism, and stress or inflammation.

Because phospholipids are often modified by reactive aldehydes that accumulate in the absence of ALDH2, we analyzed abundances of various phospholipids. Here again, livers of ASKO mice had substantially higher levels of all investigated phospholipids, including ≥2-fold increase in 26% of phosphatidylethanolamine (PE) lipid types and ≥2-fold increase in 32% of phosphatidylserine (PS) lipid types, compared to livers of WT mice (Figures S4A–S4F). PE and PS lipid types are lipid targets of 4-HNE.[49] We also detected increased abundances of TG and diacylglyceride (DG) lipid types in the livers of ASKO mice (Figures S5A and S5B). These increases in phospholipids indicated altered lipid metabolism and oxidative stress in livers of ASKO mice. Reflective of metabolites related to aldehyde in ALDH2 deficiency, we detected raised levels of four aldehydes in *Aldh2*$^{-/-}$ liver tissues, with a greater and more significant increase in ASKO mice compared to WT mouse livers (Figure S5C; $p < 0.01$).

Targeting SPTBN1 blocks metabolic and fatty liver disease caused by ALDH2 deficiency

Our results show that global *Sptbn1*$^{+/-}$ exacerbated liver phenotypes of global *Aldh2*$^{-/-}$, and a previous study showed that alcohol increased malondialdehyde in liver tissues of *Sptbn1*$^{+/-}$ mice.[37] Earlier, we found increased expression of SPTBN1 in single-cell RNA-seq analyses of human MASH/HCCs.[45] Moreover, siRNA targeting of SPTBN1 is an effective treatment for diet-induced MASH and limits the severity of chemically induced HCC.[45] Therefore, we explored the therapeutic effect of siRNA-mediated knockdown of SPTBN1 in *Aldh2*$^{-/-}$ mice. Using hydrodynamic tail-vein injection, we administered siRNA targeting SPTBN1 or a control siRNA into 10-month-old *Aldh2*$^{-/-}$ and ASKO mice fed on an NC diet. We confirmed that siSptbn1 treatment via hydrodynamic tail-vein injection specifically decreased liver SPTBN1 levels, but not in other tissues (Figures S6A and S6B).

We analyzed liver phenotypes and metabolic phenotypes at the end of a 7-week siRNA treatment with four injections of either control siRNA or siSptbn1 (Figure 2A). Liver phenotypes were significantly improved in the *Aldh2*$^{-/-}$ and ASKO mice treated with siSptbn1, liver architecture was restored, and lipid accumulation was reduced (Figures 2B and 2C). Circulating TGs in the *Aldh2*$^{-/-}$ mice were also significantly reduced after siSptbn1 treatment (Figure 2D; $p < 0.05$). However, treatment with siSptbn1 did not significantly affect liver weight and circulating ALT levels in *Aldh2*$^{-/-}$ mice (Figure 2D). Although siSptbn1 treatment did not significantly affect the body weight of *Aldh2*$^{-/-}$ mice, it significantly reduced fat weight (Figure 2D) and improved fibrosis (Figures S6C and S6D). Although blood glucose concentrations of *Aldh2*$^{-/-}$ mice were not significantly affected by siSptbn1 treatment, improved responses to GTT (Figure 2E, $p < 0.05$) and increased insulin sensitivity in an ITT (Figure S6E, $p < 0.01$) were observed after siSptbn1 treatment. MASH is associated with the activation of hepatic stellate cells,[50] which produce α-smooth muscle actin (α-SMA) and secrete collagen. We found that siSPTBN1 (25 nM) treatment of this human three-dimensional (3D)-culture MASH model reduced the amount of staining for α-SMA and collagen type I, indicators of inflammation-induced fibrosis associated with MASH (Figures 2F and 2G). Similarly, siSPTBN1 dose-dependently decreased the expression of genes involved in inflammation and fibrosis in a human 3D-culture MASH model[45] (Figures 2H and S6F).

Next, we intercrossed *Aldh2*$^{-/-}$ mice with liver-specific βII-spectrin conditional knockout mice (*Sptbn1*^{LSKO}) to generate

arrows in EM showing areas of collagen deposition. H&E and Sirius red staining were performed on formalin-fixed paraffin-embedded (FFPE) sections, and Oil Red O staining was performed on frozen sections. Scale bars represent 50 μm for H&E, 20 μm for Oil Red O, 20 μm for Sirius red, and 500 μm for EM. (J) Quantification of lipid droplet area and Sirius red staining area in WT, *Sptbn1*$^{+/-}$, *Aldh2*$^{-/-}$, and ASKO mice (n = 3–5). *$p < 0.05$, **$p < 0.01$.
See also Figures S1 and S2.

Table 1. Significantly different pathways identified by metabolomic or lipidomic analysis of livers of *Aldh2*$^{-/-}$ and ASKO mice

	Aldh2$^{-/-}$ vs. WT	ASKO vs. *Aldh2*$^{-/-}$
Metabolomics	• fatty acid activation • pyrimidine metabolism • *de novo* fatty acid synthesis • phosphatidylinositol phosphate metabolism • vitamin D3 metabolism • C21-steroid hormone biosynthesis and metabolism • prostaglandin formation from arachidonate • limonene and pinene degradation	• fatty acid oxidation, peroxisome • amino sugars metabolism • glycolysis and gluconeogenesis • methionine, cysteine, tyrosine, purine metabolism • glutathione metabolism • putative anti-inflammatory metabolites • aspartate and asparagine metabolism • glycosphingolipid biosynthesis • trihydroxycoprostanoyl-CoA β-oxidation • nitrogen metabolism • β-alanine metabolism • pentose phosphate pathway • pentose and glucuronate Interconversions • vitamin B1 metabolism • vitamin C and aldarate metabolism • vitamin D metabolism • chondroitin sulfate degradation • glyoxylate and dicarboxylate metabolism • D4- and E4-neuroprostane formation
Lipidomics	• omega-6 fatty acid metabolism • tryptophan metabolism • C21-steroid hormone biosynthesis and metabolism	• glycolysis and gluconeogenesis • pentose phosphate pathway • purine metabolism • pyrimidine metabolism • fructose and mannose metabolism • vitamin C and aldarate metabolism • carbon fixation • methionine and cysteine metabolism • selenoamino acid metabolism • vitamin B1, B3, and B9 metabolism • tryptophan, tyrosine, arginine, and proline metabolism • glutathione metabolism • valine, leucine, and isoleucine degradation • nitrogen metabolism • aspartate, asparagine, and β-alanine metabolism • butanoate metabolism

Only those pathways that were significantly altered (p value <0.05) are included.

Aldh2$^{-/-}$*Sptbn1*^{LSKO} mice. We observed a significant improvement in liver architecture and decreased microvesicular and macrovesicular lipid droplet accumulation within hepatocytes and decreased Sirius red staining in the liver of *Aldh2*$^{-/-}$*Sptbn1*^{LSKO} mice compared to *Aldh2*$^{-/-}$ mice on a WD (Figures 2I–2K, S6G, and S6H). *Aldh2*$^{-/-}$*Sptbn1*^{LSKO} mice displayed significantly decreased concentration of blood glucose and improved glucose handling, as shown by GTT (Figure 2K). Our *ex vivo* lipolysis analysis showed a significant decrease in fatty acid and glycerol release in eWAT originating from *Aldh2*$^{-/-}$*Sptbn1*^{LSKO} mice compared to *Aldh2*$^{-/-}$ mice (Figure S2E). Water intake was increased in *Aldh2*$^{-/-}$ mice receiving siSptbn1, but food intake and urine output were not significantly affected (Figure S6I).

Without ALDH2, reactive aldehyde 4-HNE accumulates in the liver, modifying and cleaving SPTBN1, forming toxic adducts with cleaved SPTBN1 fragments

Aldh2$^{-/-}$ and ASKO mice had increased linolenic acid ethyl ester, a precursor of 4-HNE,[51] in the liver (Figure S5C). We therefore investigated whether 4-HNE increased in mice deficient in ALDH2 and whether modification of SPTBN1 by 4-HNE contributed to increased lipid accumulation in the livers of these mice.

We observed increased 4-HNE levels in fixed liver sections from *Aldh2*$^{-/-}$ and ASKO mice, especially in the nucleus (Figures 3A and 3B), which result from proteins modified by 4-HNE. Liver tissue fractionation analysis also indicated that ASKO mice have higher 4-HNE adducts in the nucleus (Figure 3C). We quantified both free 4-HNE and 4-HNE-modified proteins in liver tissues. We found significantly reduced amounts of free 4-HNE in ASKO mouse livers (Figure 3D; $p < 0.001$) and slightly increased mean concentration of 4-HNE-modified proteins compared to WT mouse livers (Figure 3D). These results indicated that the increased 4-HNE labeling corresponded to an increase in 4-HNE modification of proteins. Knocking down *Aldh2* in HepG2/Huh7 cells increased 4-HNE-protein adducts in a dose-dependent manner, similar to exposing the cells to 4-HNE (Figures 3E, S7A, and S7B).

4-HNE induces SPTBN1 cleavage in a time-dependent manner, with the highest cleavage observed at 5 h after

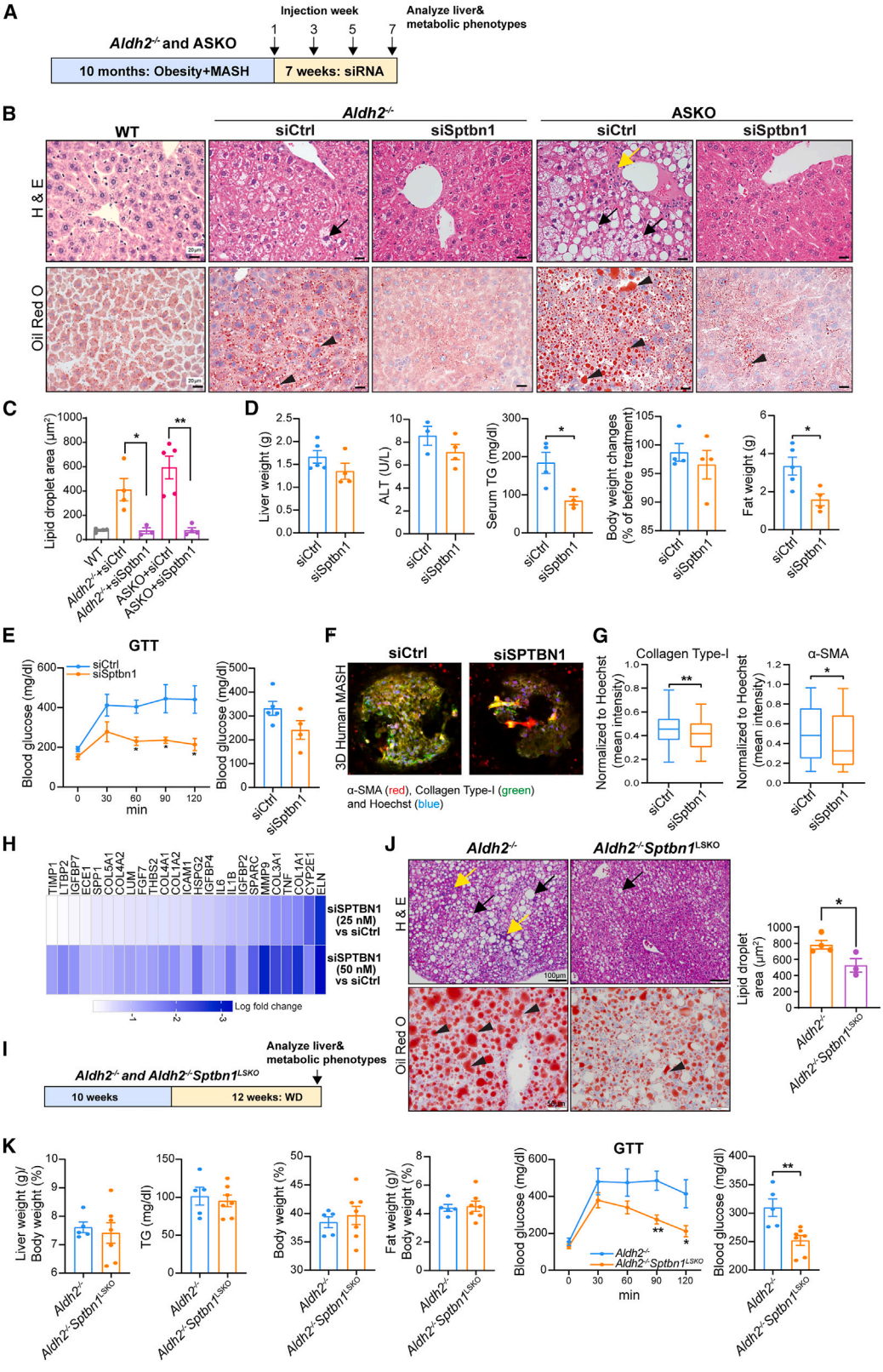

(legend on next page)

treatment (Figure 3F). 4-HNE-induced SPTBN1 cleavage is similar to the effects of palmitic acid (PA) treatment in Huh7 cells (Figures S7C). PA treatment *in vitro* is used to mimic stress conditions like lipid accumulation.[45] Further, PA treatment in siAldh2 cells significantly increases SPTBN1 cleavage and activates nSREBP1 through caspase-3 (Figure S7C). To determine whether 4-HNE modified SPTBN1, we exposed HepG2 cells to 4-HNE and monitored 4-HNE modification of SPTBN1 by immunoprecipitating SPTBN1 and blotting for 4-HNE. We detected a band recognized by the antibody against 4-HNE that corresponded to full-length SPTBN1 and a smaller band that likely represented a stress-induced SPTNB1 cleavage product, N-SPTBN1 (N-terminal fragment of SPTBN1) (Figures 3G and S7D). To confirm that the smaller fragment matched the fragment generated by caspase-3 cleavage was modified by 4-HNE, we transfected a plasmid expressing either a V5-tagged N-SPTBN1 or a V5-tagged C-terminal fragment of SPTBN1 (C-SPTBN1) into Huh7 and HepG2 cells and found that only the N-SPTBN1 fragment was modified by 4-HNE (Figures 3H and S7E). Thus, these data showed that 4-HNE that accumulated in the livers of ALDH2-deficient mice modified cleaved SPTBN1.

Utilizing AlphaFold-based modeling (AlphaFold ID: Q01082), we examined the 3D structure of SPTBN1, spanning three SPTBN1 fragments (50–975, 1,132–2,155, and 2,198–2,364 amino acids), and 4-HNE (PubChem CID: 5283344), then performed structure-based molecular docking simulations. We found that Gln531, Phe534/594, Cys604, Cys1284, His1257, Lys1259, and Cys2264 are potential/likely targets for HNE reactivity (Figures 3I and S7F). Next, through mass spectrometry (MS) analysis, we confirmed that Cys1284 is modified, supporting the model's validity. We also found that other SPTBN1 residues were modified, indicating that the 4-HNE adduct may be even more pervasive than indicated by AlphaFold. Therefore, Cys1284 and Cys1389 were covalently modified by Michael addition and Schiff base addition in 4-HNE-treated cells (Figures 3J and S7G). Adducted N-SPTBN1 was distributed in the cytoplasm and the nucleus, with a higher proportion in the nucleus (Figure 3J).

Modifying cleaved SPTBN1 by 4-HNE alters TGF-β signaling, leading to abnormal pro-fibrogenic and pro-oncogenic signaling

4-HNE did not affect SPTBN1 levels but did promote SPTBN1 cleavage (Figure 3F). Because SPTBN1 is a crucial SMAD3 adaptor, we hypothesized that 4-HNE modification of SPTBN1 generating SPTBN1 fragments that formed toxic adducts with 4-HNE could alter SMAD3/TGF-β signaling. We utilized siRNA to knock down *Sptbn1* and *Aldh2* in HepG2 and LX-2 cells and then treated cells with 4-HNE. Confocal imaging showed that *Aldh2* silencing reduced the TGF-β treatment-induced SMAD3 nuclear translocation and signaling (Figures 4A, 4B, and S8A). In contrast, *Sptbn1* silencing blocked 4-HNE toxicity and restored normal SMAD3 localization and signaling (Figures 4A and 4B). By western blot, we confirmed decreased *p*-SMAD3 expression under ALDH2 knockdown condition and restoration of *p*-SMAD3 expression upon siRNA targeting SPTBN1 (Figures 4C and S8B). RNA-seq data indicated pro-fibrotic and potentially oncogenic TGF-β signaling in ASKO mice, with increased CDK4 and CCL9 expression[52] (Figure 4D), whereas,

Figure 2. Targeting SPTBN1 improves liver and metabolic phenotypes of *Aldh2*$^{-/-}$, ASKO mice, and human 3D cultures

(A) Diagram of the siRNA treatment protocol. *Aldh2*$^{-/-}$ mice that developed obesity at 10 months old were administered siSptbn1 or control siRNA (siCtrl) at a dose of 1.25 nmol/mouse. siRNA was hydrodynamically injected four times over 7 weeks.

(B) Liver histology of control WT mice not injected with any siRNA (left panel) and *Aldh2*$^{-/-}$ and ASKO mice receiving the indicated siRNA treatments (middle and right panels). Increased microvesicular lipid, macrovesicular lipid (black arrows), and inflammation (yellow arrows) are observed in H&E-stained liver tissues from *Aldh2*$^{-/-}$ and ASKO mice treated with siCtrl (top panels). Oil Red O-stained images show a high amount of fat droplets (black arrowheads) from siCtrl treated ASKO mice liver tissues compared to siSPTBN1 mouse tissues (bottom panels). Scale bars, 20 μm.

(C) Quantification results of lipid droplet area of each condition (n = 3–5). Data are presented as mean ± SEM. *p < 0.05, **p < 0.01.

(D) Graphs showing changes in liver weight, serum ALT levels, and serum TG levels in *Aldh2*$^{-/-}$ mice receiving the indicated siRNAs (n = 3–5 mice/group) as well as changes in body weight and fat weight of *Aldh2*$^{-/-}$ mice receiving the indicated siRNAs (n = 4–5 mice/group). Pairwise t tests determined statistical differences. Data are presented as mean ± SEM. *p < 0.05.

(E) Glucose handling in *Aldh2*$^{-/-}$ mice receiving the indicated siRNAs. Blood glucose levels and results of GTT are shown. Statistical differences in blood glucose were determined by pairwise t tests (n = 4–5 mice/group) and by pairwise t tests for each time point in GTT values (n = 3 mice/group). Data are presented as mean ± SEM. *p < 0.05.

(F) Representative images showing expressions of α-SMA and collagen type I, indicators of stellate cell activation, in human 3D MASH cultures exposed to siCtrl or siSPTBN1 for 96 h. Antibody recognizing α-SMA (red) or collagen (green) and nuclei were stained with Hoechst (blue).

(G) Intensities of collagen type I and α-SMA normalized to the Hoechst intensity and presented as mean intensity ± SEM (n = 112–168 data points from eight sections of the culture). Statistically significant differences were determined by pairwise t tests. *p < 0.05, **p < 0.01.

(H) Heatmap of the log-fold differences in transcripts associated with inflammation or fibrosis in human 3D MASH cultures exposed to siRNA targeting SPTBN1 compared to those exposed to control siRNA. Results for two concentrations of siSPTBN1 are shown. Triplicate cultures were exposed to the siRNAs for 96 h.

(I) Diagram of the Western diet treatment protocol in *Aldh2*$^{-/-}$ control mice and *Aldh2*$^{-/-}$*Sptbn1*^{LSKO} mice.

(J) Liver histology of *Aldh2*$^{-/-}$ control mice and *Aldh2*$^{-/-}$*Sptbn1*^{LSKO} mice receiving the Western diet (WD) treatment. Left: microvesicular lipid, macrovesicular lipid (black arrows), and inflammation (yellow arrows) are indicated on the H&E-stained images (top panels). Oil Red O-stained images showing fat droplets (black arrowheads) from WD-fed *Aldh2*$^{-/-}$ and *Aldh2*$^{-/-}$*Sptbn1*^{LSKO} mouse tissues (bottom panels). Scale bars represent 100 μm for H&E and 50 μm for Oil Red O. Right: quantification of lipid droplet and Sirius red staining of each genotype (n = 3–4). *p < 0.05. Quantification results of lipid droplet area in *Aldh2*$^{-/-}$ and *Aldh2*$^{-/-}$*Sptbn1*^{LSKO} mice (n = 3–4). Data are presented as mean ± SEM. *p < 0.05.

(K) *Aldh2*$^{-/-}$*Sptbn1*^{LSKO} mice show significantly better glucose handling compared to *Aldh2*$^{-/-}$ mice. The graphs show liver weight, serum TG, body weight, fat weight, and glucose handling in *Aldh2*$^{-/-}$ control mice and *Aldh2*$^{-/-}$*Sptbn1*^{LSKO} mice. Statistical differences were determined by pairwise t tests (n = 5–7 mice/group). Data are presented as mean ± SEM. *p < 0.05, **p < 0.01.

See also Figure S6.

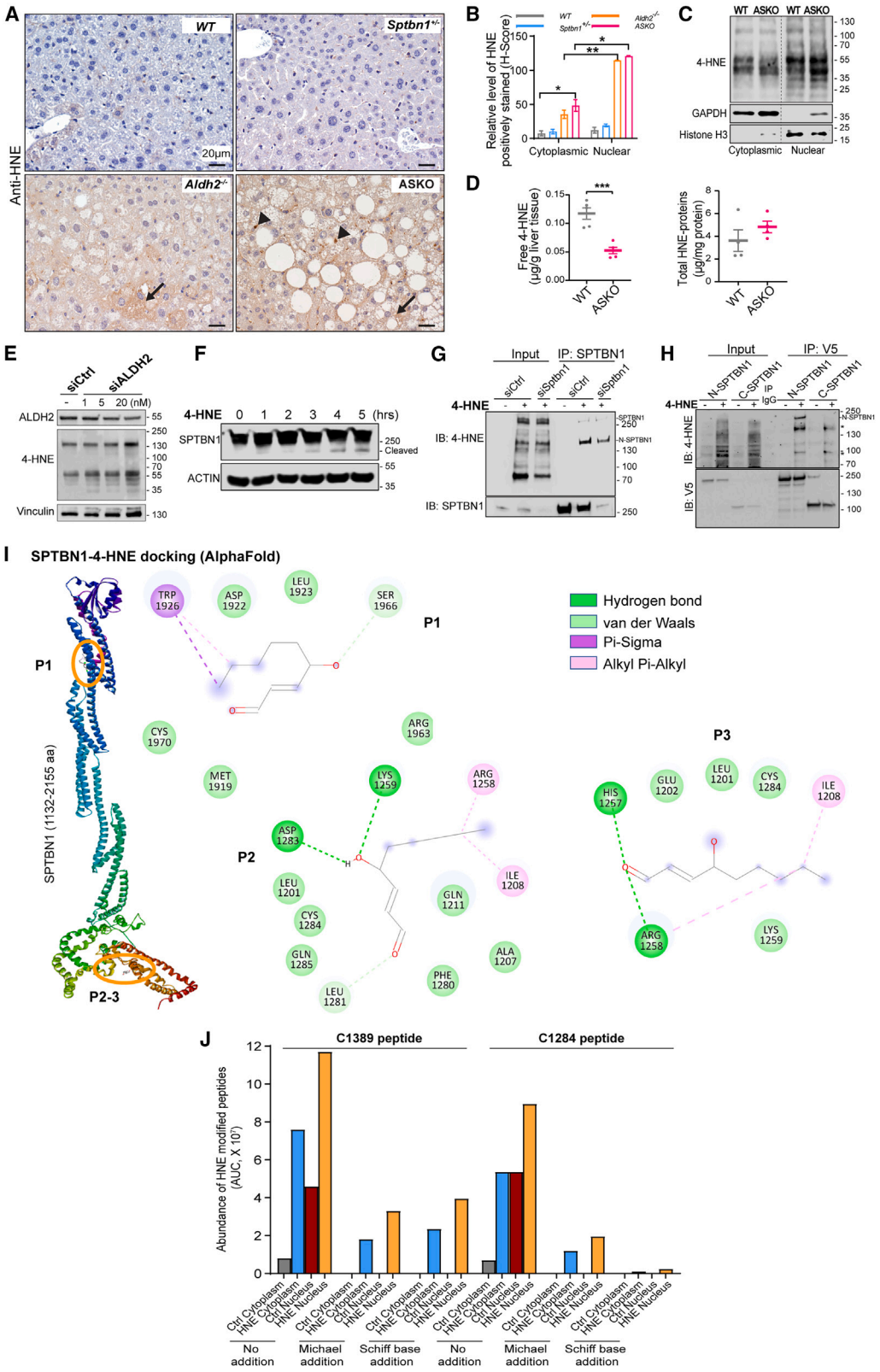

(legend on next page)

mouse liver-specific knockout of *Sptbn1* reversed oncogenic TGF-β signaling (Figure 4D).

To further explore whether ASKO mice with phenotypes resembling MetS and MASLD/MASH are more susceptible to HCC development, we used a chemically induced HCC mouse model using diethylnitrosamine (DEN) plus WD feeding (Figure 5A). We evaluated liver tumor development within 10 months and found that single injection of DEN plus WD feeding induced a significantly greater frequency of liver tumors in *Aldh2*$^{-/-}$ mice and ASKO mice (Figure 5B). Compared to WT mice, ASKO mice demonstrated an increase in body weight and liver weight, and higher visibility of tumor nodules (Figures 5C–5E). In contrast, blocking SPTBN1 in *Aldh2*$^{-/-}$ mice (*Aldh2*$^{-/-}$ *Sptbn1*^{LSKO}) developed smaller and fewer tumors.

We also examined liver tissues for markers of immune cell types regulated by TGF-β, such as F4/80, CD4, FoxP3, and CD11b.[53] Using immunofluorescent staining, we observed markedly increased CD11b^{+} monocyte infiltrations in ASKO liver tissues compared to WT mice (Figures S9A and S9B). These data indicated that ASKO mouse liver tissues recruited more monocytes to promote MASH progression. Together, these studies demonstrated that under conditions of reduced ALDH2, toxic reactive aldehydes accumulate and partner with cleaved SPTBN1 fragments, resulting in a toxic alteration of TGF-β signaling and promoting a fibrogenic and oncogenic phenotype that is restored to normal by complete inhibition of SPTBN1. This is depicted in a model that we propose (Figure 6).

DISCUSSION

Genetic variations in *ALDH2* and *SPTBN1* are associated with health issues in the human population. Function-compromising variants in ALDH2 among individuals are associated with increased risk for multiple disorders and alcohol-associated cancers.[54,55] *SPTBN1* haploinsufficiency is associated with neurodevelopmental syndromes,[56] and a specific point mutation in SPTBN1 is associated with HCC.[46] By evaluating SNPs in obese or healthy-weight individuals, we have identified an intronic SNP (rs968529) in *ALDH2* associated with obesity. Our SNP analysis also identifies a significant association between an intronic *SPTBN1* variant (rs2941583) and obesity. Although the threshold for significance was low, we also identified a pair of SNPs in *SPTBN1* (rs7599241 and rs17046097) that are present in both the obese group and patients with either MASLD or MASH.

These SNPs are in intronic regions and present in regions of the genetic loci that encode multiple products. Thus, the impact of these variants on ALDH2 or SPTBN1 function or abundance in the liver remains to be investigated. However, expression analysis indicated that the *ALDH2* SNP rs968529 and the *SPTBN1* SNP rs2941483 could affect tissue-specific gene expression. Additionally, the *SPTNB1* SNP rs2941483 is associated with RAD21, a protein part of the multifunctional chromatin-regulating cohesin complex.[57] Furthermore, the *SPTBN1* SNP rs7599241 is also associated with hypertension in a Korean cohort.[58] Given the clinical associations among obesity, hypertension, MASLD, and MASH,[10,59] the *SPTBN1* SNP rs7599241 could play a significant role in these diseases.

The activity of ALDH2 is lost in our *Aldh2*$^{-/-}$ mouse model on a normal diet, resulting in an abnormal accumulation of reactive aldehydes that aberrantly partner with cleaved fragments of the SMAD3/4 adaptor SPTBN1, disrupting normal SPTBN1-SMAD3 signaling. Our mechanistic investigation demonstrates an alteration of the normal functioning of this SMAD3/4-SPTBN1 complex by the 4-HNE-SPTBN1 adducts, altering TGF-β signaling, thereby promoting injury and lipogenesis that ultimately manifests as MetS and cancer (Figure 6). In this scenario, the key challenge to treat these diseases is to efficiently target well-defined molecules in a non-toxic and safe way. Strikingly, targeting SPTBN1 in mouse models of obesity and MASH blocked interactions between reactive aldehydes and SREBP1,

Figure 3. SPTBN1 is modified by 4-HNE

(A) Representative image of 4-HNE immunohistochemistry in the liver tissue from 44–48-week-old WT, *Sptbn1*$^{+/-}$, *Aldh2*$^{-/-}$, and ASKO mice, respectively. Increased 4-HNE adducts are observed in ASKO mice compared to WT. Cytoplasmic staining is indicated by arrows, while nuclear staining is denoted by the arrowhead. Staining was performed on FFPE tissue sections. Scale bars, 20 μm.

(B) Quantification of cytoplasmic and nuclear HNE adducts in WT, *Sptbn1*$^{+/-}$, *Aldh2*$^{-/-}$, and ASKO mice, respectively (n = 2). Data are presented as mean ± SEM. $^{*}p < 0.05$, $^{**}p < 0.01$.

(C) Western blot analysis of cytoplasmic and nuclear HNE adducts in WT and ASKO mice.

(D) Quantification of free (left) and protein-bound (right) 4-HNE in liver tissue of WT and ASKO mice (44–48 weeks old). Statistically significant differences were determined by pairwise t test (n = 4–5/group). Data are presented as mean ± SEM. $^{***}p < 0.001$.

(E) siRNA-mediated silencing of Aldh2 increases 4-HNE protein adducts. Lysates from HepG2 cells exposed to either control siRNA (siCtrl) or siRNA targeting ALDH2 (siAldh2 0, 1, 5, and 20 nM) were immunoblotted with an antibody recognizing 4-HNE.

(F) Western blot analysis of SPTBN1 cleavage at different time points after HNE treatment (20 μM, every hour adding 4-HNE) in HepG2 cells. The cleaved N-SPTBN1 fragment is indicated on the right.

(G) Detection of 4-HNE-SPTBN1 adduct through immunoprecipitation analysis. LX-2 were treated with 4-HNE (40 μM) for 3 h. Immunoblot (IB): full-length SPTBN1 and the N-terminal fragment (N-SPTBN1) are indicated. Negative control: siSptbn1 treatment group; SPTBN1 IP, SPTBN1 immunoprecipitation.

(H) Detection of 4-HNE on N-SPTBN1 adducts in Huh7 cells expressing either V5-tagged N-SPTBN1 or C-SPTBN1 upon exposure to 20 μM 4-HNE for 4 h. IgG IP, immunoglobin G immunoprecipitation (negative control); IP: V5, immunoprecipitation with antibody recognizing V5; IB, immunoblot. N-SPTBN1 is indicated, and asterisks indicate non-specific bands.

(I) Identification of potential 4-HNE binding sites in SPTBN1 through molecular docking analysis. Cartoon representation showing hydrogen bonds and hydrophobic interactions formed between 4-HNE and SPTBN1 fragment (Q1132-T2155). Interacting amino acid residues in SPTBN1 are indicated by a 3-letter code.

(J) Confirmation of the 4-HNE binding sites in spectrin via mass spectrometry analysis. 4-HNE-modified peptide containing Cys1389 and Cys1284 is indicated on the top. Abundance of 4-HNE-modified peptides in nuclear and cytoplasmic fractions is depicted on the x axis.

See also Figure S7.

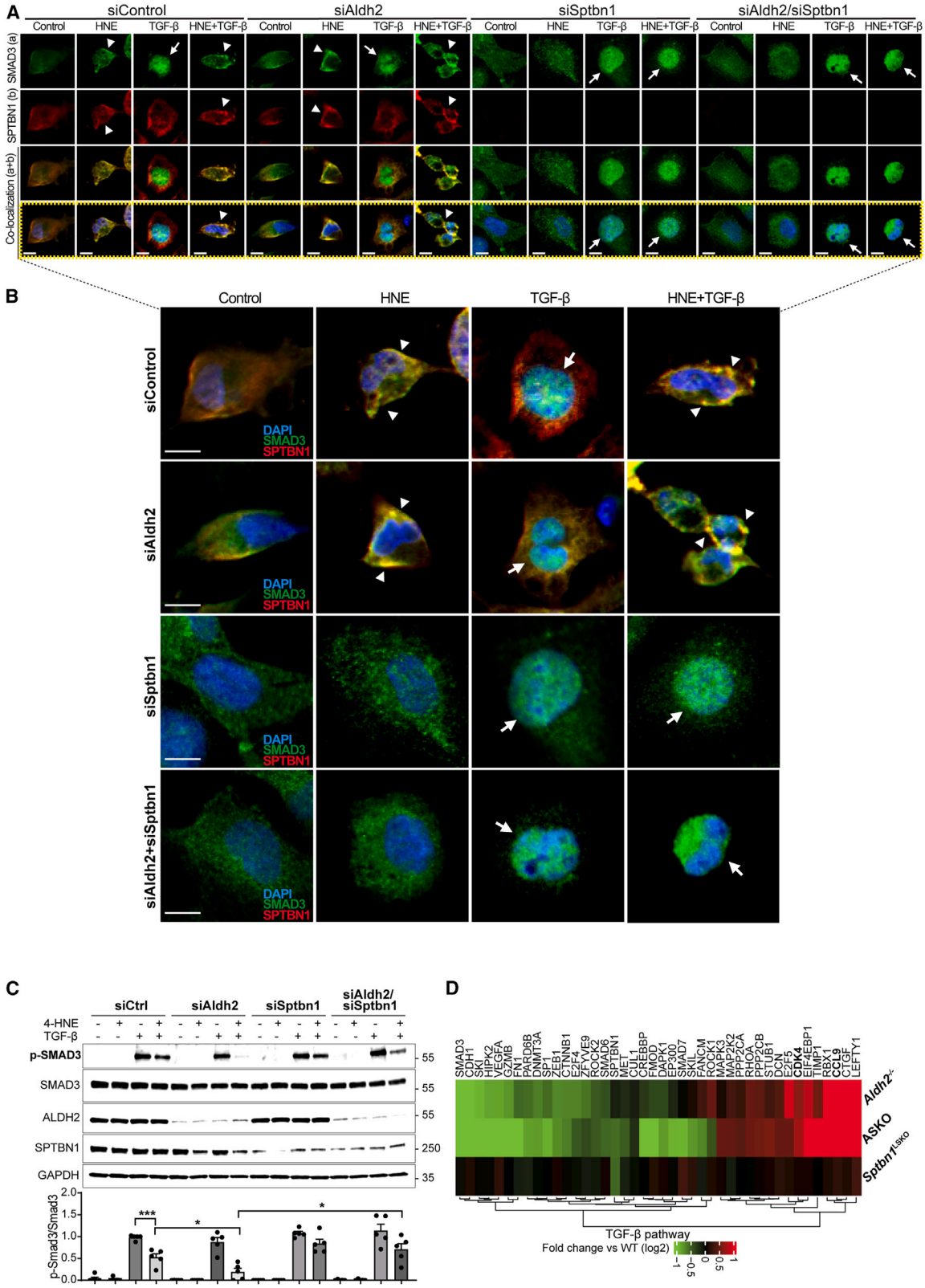

(legend on next page)

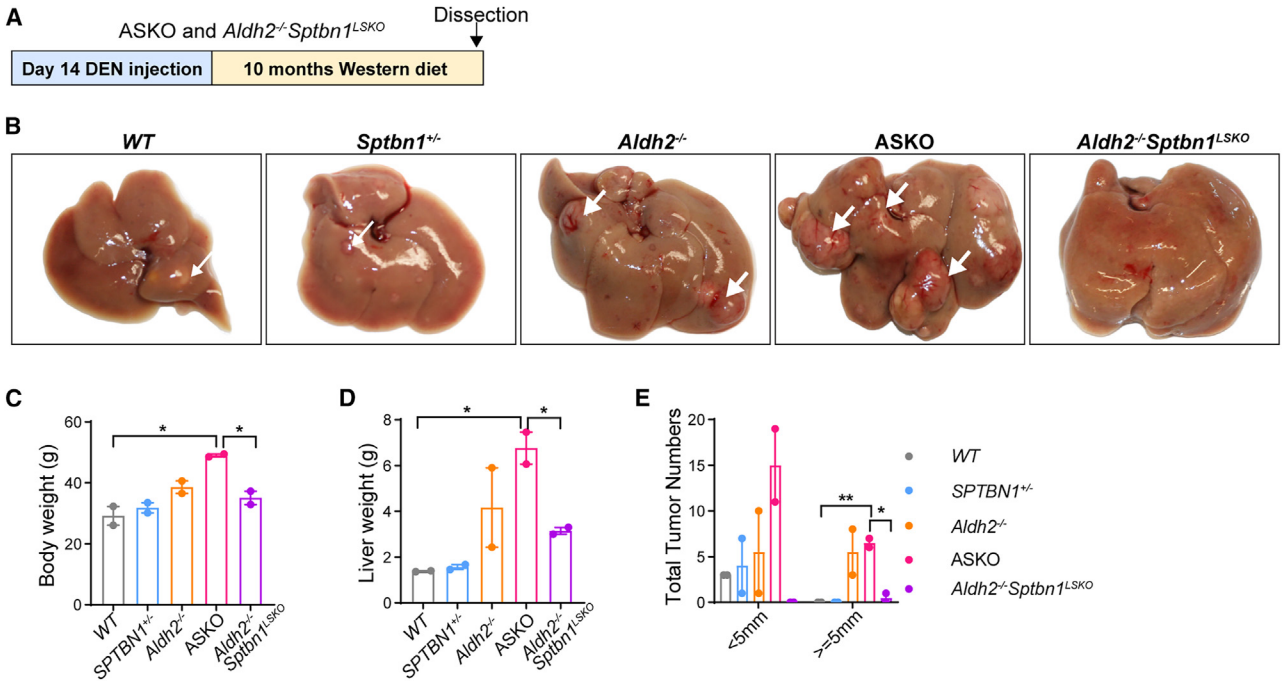

Figure 5. *Aldh2*$^{-/-}$ mice and ASKO mice injected with diethylnitrosamine (DEN) and on WD demonstrate severe liver injury

(A) Diagram of the experimental procedure of chemical (DEN) plus WD-induced HCC (top).

(B) Gross morphology of livers in WT, *Sptbn1*$^{+/-}$, *Aldh2*$^{-/-}$, and ASKO mice 10 months after DEN and WD. Inflammation (white arrows) sites are indicated.

(C and D) Graphs show different values of body weight and liver weight of WT, *Sptbn1*$^{+/-}$, *Aldh2*$^{-/-}$, and ASKO mice 10 months after DEN and WD. *$p < 0.05$.

(E) Number of visible liver nodules (<5 mm and ≥5 mm) in the liver tissues from WT, *Sptbn1*$^{+/-}$, *Aldh2*$^{-/-}$, and ASKO mice 10 months after DEN and WD. *$p < 0.05$, **$p < 0.01$.

without toxicities, and significantly halted progression of MASH fibrosis, lipid accumulation, and tissue damage in the liver. This treatment approach also caused normalization of the liver immune phenotypes and cell types regulated by TGF-β, such as CD4$^+$, FoxP3$^+$, CD11b$^+$, and F4/80$^+$ cells. Collectively, our data indicate that SPTBN1 is a potential target for treating MetS and MASLD and MASH associated with MetS. ASKO mice exhibit characteristics of MetS, such as obesity, excess visceral fat, poor glucose handling, and MASLD with progression to MASH. Our results suggest that ASKO mice represent powerful and useful models for studying these conditions.

Similar to previous studies of *Aldh2*$^{-/-}$ mice[60] or *Sptbn1*$^{+/-}$ mice,[37] our metabolomic analyses show increased precursors of reactive aldehydes in the livers of both genotypes of ALDH2-deficient mice. Findings that SPTBN1 is modified by 4-HNE and that protein-associated 4-HNE is increased in the livers of the mutant mice suggest an important mechanism for MASH that developed in these mice. Previously, we have shown that SPTBN1 is cleaved by caspase-3, and the N-terminal cleavage product stabilizes the active cleaved form of SREBP1.[45] With molecular docking simulations, we predicted two sites where 4-HNE could bind and potentially modify cleaved fragments of SPTBN1. These studies were confirmed by MS analyses showing modifications of cleaved spectrin by 4-HNE. Moreover, our studies indicate that 4-HNE modification and such aldehyde modifications cleave and disrupt SPTBN1 function, particularly its role as a SMAD3 adaptor, with SPTBN1-4-HNE toxic adducts altering TGF-β signaling, addressing an important next step in their role as signaling agents.[7] Here also, SPTBN1 appears to serve as an integrator of stress signals in hepatocytes. The data demonstrated that reducing the abundance of SPTBN1 cleavage products has a beneficial effect by

Figure 4. 4-HNE alters TGF-β signaling to a pro-fibrotic and oncogenic phenotype

(A and B) Effects of 4-HNE on the SMAD3 nuclear translocation in LX-2 cells transfected with siCtrl or siAldh2 or siSptbn1 examined by confocal microscopy imaging. White arrowheads indicate accumulation of SPTBN1and SMAD3 on the cell membrane. White arrows indicate SMAD3 nuclear localization. Scale bar, 20 μm.

(C) Western blot of the indicated proteins in HepG2 cells treated with indicated siRNA (sequentially silence ALDH2 and SPTBN1) and exposed to 4-HNE (20 μM) or TGF-β (200 pM). Representative image of five repeated western blot experiments (top panel). Quantification of pSmad3 from five independent experiments (bottom panel). Data are presented as mean ± SEM. *$p < 0.05$, ***$p < 0.001$.

(D) Heatmap shows fold changes in expressions of genes involved in the TGF-β signaling in liver tissues of *Aldh2*$^{-/-}$, ASKO, and *Sptbn1*^{LSKO} mice vs. WT mice with significant difference by bulk RNA-seq.

See also Figure S8.

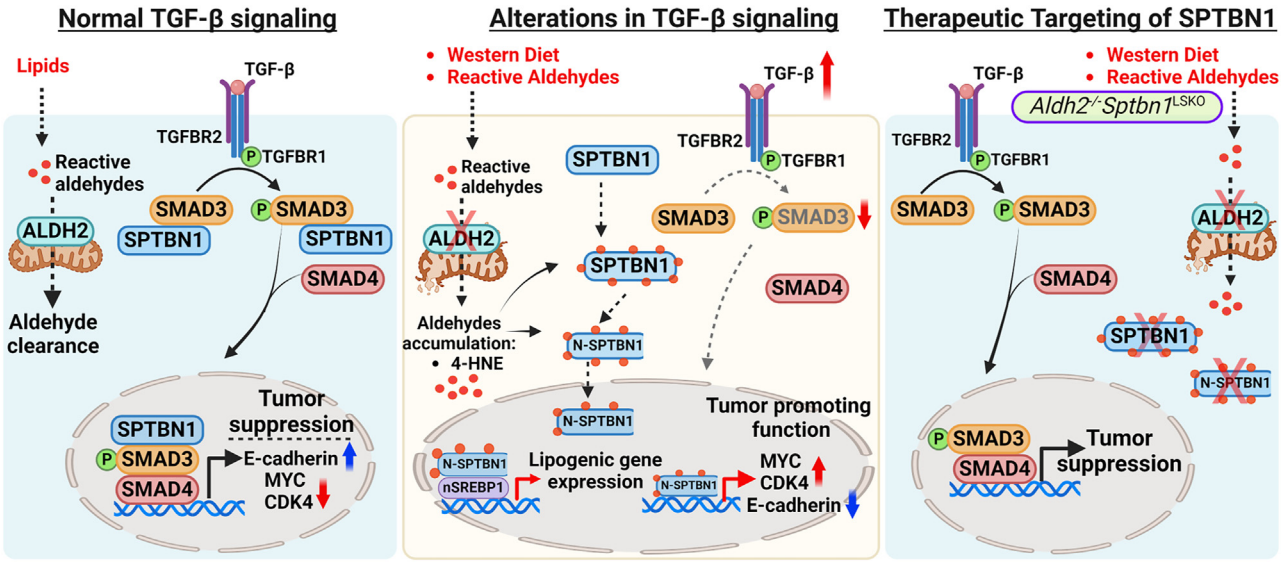

Figure 6. Schematic representation of how aldehydes modify SPTBN1 and disrupt normal SPTBN1/Smad3/TGF-β signaling in ALDH2 deficiency, causing fibrosis and disease

(Left) Normal regulation of lipid and energy homeostasis. Normal ALDH2 levels and intact transforming growth factor β (TGF-β)/Smad3/SPTBN1 signaling suppress obesity, fibrosis, and cancer by directly targeting PAI-1, CTGF, c-Jun, CDK4, and others.

(Middle) Reduced activity of ALDH2 and haploid SPTBN1 (as in our ASKO mouse model on a normal diet) leads to an abnormal accumulation of reactive aldehydes that aberrantly partner with cleaved fragments of the SMAD3/4 adaptor SPTBN1, disrupting normal SPTBN1-SMAD3 signaling. Subsequent alterations in the normal functioning SMAD3/4-SPTBN1 complex by the 4-HNE-SPTBN1 adducts alter TGF-β signaling, promoting injury, lipogenesis, and oncogenesis, ultimately manifesting in metabolic syndrome and cancer.

(Right) Our proposed therapeutic targets, particularly targeting SPTBN1 in mouse models of obesity and metabolic dysfunction-associated steatohepatitis (MASH), have significant potential. Our research has shown that this approach can effectively block SPTBN1 cleavage and interactions between reactive aldehydes, thereby significantly halting the progression of MASH fibrosis, lipid accumulation, and tissue damage in the liver.

limiting steatosis-inducing changes in lipid metabolism and blocking fibrosis-inducing changes in hepatic stellate cells. While treatment strategies based on the catalytic activity of enzymes such as ALDH2 are attractive and could potentially correct physiological functions, challenges such as lack of specificity, off-target events, and immune reactions against the enzyme render these strategies elusive to date in clinical trials. Collectively, our studies demonstrate that targeting SPTBN1 is a potentially significant and important non-toxic approach to achieving a beneficial response in patients with MetS or those in early stages of MASH as well as in preventing cancer.

Limitations of the study

Our study demonstrates how the accumulation of aldehydes produced by a WD disrupts TGF-β signaling, a major pathway in disease and cancer. The mechanism implements toxic cleavage and adduct formation with the SMAD3 adaptor SPTBN1, exacerbated by a functional deficiency of ALDH2. Significantly, blocking SPTBN1 cleavage inhibits the development of fatty liver disease and cancer. However, a limitation is that this study does not address the systemic effects of the aldehydes. In addition, nearly half a billion people have a functional deficiency of ALDH2. While this deficiency is associated with liver disease and cancer, the study does not address other effects that are associated with ALDH2 deficiency. Because our study focused on MASLD, MASH, and HCC, signals from the liver are also likely involved in systemic functions in patients with these disorders. Tissue specificity of insulin resistance and glucose handling, as well as clinical studies, are aspects that require further investigation and are limitations of our study. The study is limited by an in-depth mechanism of how the adducts alter normal SMAD3 signaling. While we determined immune cell types regulated by TGF-β, such as F4/80, CD4, FoxP3, and CD11b, we did not address the functional roles of these cells using extensive mouse experiments, and these warrant further studies in the future.

RESOURCE AVAILABILITY

Lead contact

Further information and requests for resources and reagents should be directed to and will be fulfilled by the lead contact, Lopa Mishra (lopamishra2@gmail.com).

Materials availability

This study did not generate new unique reagents.

Data and code availability

- Metabolomics, lipidomics, mass spectrometry, and RNA sequencing data have been deposited at National Metabolomics Data Repository (NMDR), ProteomeXchange Consortium, and GEO repository and are publicly available as of the date of this publication using the accession number provided in the key resources table. An Excel file including source data has been deposited in Mendeley Data and is publicly available under the following site: DOI: 10.17632/nrpm8ydybr.1.
- This paper does not report original code.

- Additional information required to reanalyze the data reported in this paper is available from the lead contact upon request.

ACKNOWLEDGMENTS

We thank Dr. Agata Smogorzewska from Rockefeller University for the *Aldh2*$^{-/-}$ mice. We thank Drs. Zhanhuai Wang, Sobia Zaidi, and Wilma Jogunoori for technical support. We thank Dr. Gareth Guenigault's support with assays in the 3D human MASH co-culture model. We thank Dr. Nancy R. Gough for intellectual input and manuscript editing. This research was supported by National Institutes of Health, United States - NIH/NIAAA grant R01AA023146(L.M.), NIH/NCI grants R01CA236591 (L.M.), U01CA230690 (L.M.), and an Elaine H. Snyder Cancer Research award (L.M.).

AUTHOR CONTRIBUTIONS

L.M. conceived the study and hypotheses, supervised the research, and wrote the manuscript. X.Y., K.B., and S.R. designed the experiments, performed *in vitro* assays and *in vivo* animal studies, analyzed the data, and contributed to manuscript preparation. X.X. performed bioinformatics analysis of RNA-seq data and *in vitro* assays. K.O. generated plasmids and performed *in vitro* assays and edited the manuscript. R.L.A. performed biostatistical analyses. P.C. and K.O. performed MS analysis. J.R.M. and S.K.L. performed and analyzed the CT scans. Md.I.H., T.M., and K.B. performed molecular docking simulations. A.K.V. and H.H. proofread and edited the manuscript. S.J. performed immunohistochemistry and edited the manuscript. P.S.L. provided intellectual input and analyzed the immunohistochemical labeling slides. K.S., S.K.L., J.M.C., B.M., S.D., X.W.W., K.C., and A.R.K. provided intellectual input. H.Y. and Z.W. performed SNP analysis.

DECLARATION OF INTERESTS

The authors declare no competing interests.

STAR★METHODS

Detailed methods are provided in the online version of this paper and include the following:

- KEY RESOURCES TABLE
- EXPERIMENTAL MODEL AND STUDY PARTICIPANT DETAILS
  - Husbandry, diets, and dietary intervention in mice
  - Patient samples for single-nucleotide polymorphism analysis
- METHOD DETAILS
  - Cell lines
  - Single-nucleotide polymorphism determination and statistical analysis for association with obesity or liver disease
  - Hydrodynamic *in vivo* siRNA targeting
  - Measurements of serum triglycerides (TGs), glucose, insulin, and liver enzyme (ALT)
  - Glucose tolerance test (GTT) and insulin tolerance test (ITT)
  - Immunoblotting and co-immunoprecipitation (IP) analyses
  - CT scan
  - Measurements of liver, visceral fat, and tissue histology
  - Measurement of *ex vivo* lipolysis
  - Measurements of food intake, water intake, and urine output
  - Immunofluorescence analyses
  - Multiplex immunofluorescence staining
  - Human 3D MASH culture and analysis
  - RNA extraction, RNA sequencing, and pathway analysis
  - Metabolomic and lipidomic analyses
  - Structure modeling and molecular docking simulations with SPTBN1 and 4-HNE
  - Quantification of free 4-HNE by mass spectrometry
  - snRNA-seq
  - Quantitative PCR
- QUANTIFICATION AND STATISTICAL ANALYSIS

SUPPLEMENTAL INFORMATION

Supplemental information can be found online at https://doi.org/10.1016/j.celrep.2024.114676.

Received: January 24, 2024
Revised: June 24, 2024
Accepted: August 8, 2024

REFERENCES

1. Harrison, S.A., Allen, A.M., Dubourg, J., Noureddin, M., and Alkhouri, N. (2023). Challenges and opportunities in NASH drug development. Nat. Med. *29*, 562–573. https://doi.org/10.1038/s41591-023-02242-6.
2. de la Fuente, M., Lombardero, L., Gomez-Gonzalez, A., Solari, C., Angulo-Barturen, I., Acera, A., Vecino, E., Astigarraga, E., and Barreda-Gomez, G. (2021). Enzyme Therapy: Current Challenges and Future Perspectives. Int. J. Mol. Sci. *22*. https://doi.org/10.3390/ijms22179181.
3. Dingler, F.A., Wang, M., Mu, A., Millington, C.L., Oberbeck, N., Watcham, S., Pontel, L.B., Kamimae-Lanning, A.N., Langevin, F., Nadler, C., et al. (2020). Two Aldehyde Clearance Systems Are Essential to Prevent Lethal Formaldehyde Accumulation in Mice and Humans. Mol. Cell. *80*, 996–1012.e9. https://doi.org/10.1016/j.molcel.2020.10.012.
4. Goldin, A., Beckman, J.A., Schmidt, A.M., and Creager, M.A. (2006). Advanced Glycation End Products. Circulation *114*, 597–605. https://doi.org/10.1161/CIRCULATIONAHA.106.621854.
5. Chapple, S.J., Cheng, X., and Mann, G.E. (2013). Effects of 4-hydroxynonenal on vascular endothelial and smooth muscle cell redox signaling and function in health and disease. Redox Biol. *1*, 319–331. https://doi.org/10.1016/j.redox.2013.04.001.
6. Chen, Z., Tian, R., She, Z., Cai, J., and Li, H. (2020). Role of oxidative stress in the pathogenesis of nonalcoholic fatty liver disease. Free Radic. Biol. Med. *152*, 116–141. https://doi.org/10.1016/j.freeradbiomed.2020.02.025.
7. Pham, V.N., Bruemmer, K.J., Toh, J.D.W., Ge, E.J., Tenney, L., Ward, C.C., Dingler, F.A., Millington, C.L., Garcia-Prieto, C.A., Pulos-Holmes, M.C., et al. (2023). Formaldehyde regulates S-adenosylmethionine biosynthesis and one-carbon metabolism. Science *382*, eabp9201. https://doi.org/10.1126/science.abp9201.
8. Wang, H.H., Lee, D.K., Liu, M., Portincasa, P., and Wang, D.Q.-H. (2020). Novel Insights into the Pathogenesis and Management of the Metabolic Syndrome. Pediatr. Gastroenterol. Hepatol. Nutr. *23*, 189–230. https://doi.org/10.5223/pghn.2020.23.3.189.
9. Armani, A., Berry, A., Cirulli, F., and Caprio, M. (2017). Molecular mechanisms underlying metabolic syndrome: the expanding role of the adipocyte. Faseb. J. *31*, 4240–4255. https://doi.org/10.1096/fj.201601125RRR.
10. Lonardo, A., Nascimbeni, F., Mantovani, A., and Targher, G. (2018). Hypertension, diabetes, atherosclerosis and NASH: Cause or consequence? J. Hepatol. *68*, 335–352. https://doi.org/10.1016/j.jhep.2017.09.021.
11. Huang, D.Q., El-Serag, H.B., and Loomba, R. (2021). Global epidemiology of NAFLD-related HCC: trends, predictions, risk factors and prevention. Nat. Rev. Gastroenterol. Hepatol. *18*, 223–238. https://doi.org/10.1038/s41575-020-00381-6.
12. Lin, E., Kuo, P.H., Liu, Y.L., Yang, A.C., and Tsai, S.J. (2017). Transforming growth factor-beta signaling pathway-associated genes SMAD2 and TGFBR2 are implicated in metabolic syndrome in a Taiwanese population. Sci. Rep. *7*, 13589. https://doi.org/10.1038/s41598-017-14025-4.
13. Nikolic, I., Leiva, M., and Sabio, G. (2020). The role of stress kinases in metabolic disease. Nat. Rev. Endocrinol. *16*, 697–716. https://doi.org/10.1038/s41574-020-00418-5.
14. Crabb, D.W., Edenberg, H.J., Bosron, W.F., and Li, T.K. (1989). Genotypes for aldehyde dehydrogenase deficiency and alcohol sensitivity. The

inactive ALDH2(2) allele is dominant. J. Clin. Invest. *83*, 314–316. https://doi.org/10.1172/jci113875.

15. Eng, M.Y., Luczak, S.E., and Wall, T.L. (2007). ALDH2, ADH1B, and ADH1C genotypes in Asians: a literature review. Alcohol Res. Health *30*, 22–27.
16. Guillot, A., Ren, T., Jourdan, T., Pawlosky, R.J., Han, E., Kim, S.J., Zhang, L., Koob, G.F., and Gao, B. (2019). Targeting liver aldehyde dehydrogenase-2 prevents heavy but not moderate alcohol drinking. Proc. Natl. Acad. Sci. USA *116*, 25974–25981. https://doi.org/10.1073/pnas.1908137116.
17. Zhu, Y., Zhang, D., Zhou, D., Li, Z., Li, Z., Fang, L., Yang, M., Shan, Z., Li, H., Chen, J., et al. (2017). Susceptibility loci for metabolic syndrome and metabolic components identified in Han Chinese: a multi-stage genome-wide association study. J. Cell Mol. Med. *21*, 1106–1116. https://doi.org/10.1111/jcmm.13042.
18. Spracklen, C.N., Horikoshi, M., Kim, Y.J., Lin, K., Bragg, F., Moon, S., Suzuki, K., Tam, C.H.T., Tabara, Y., Kwak, S.-H., et al. (2020). Identification of type 2 diabetes loci in 433,540 East Asian individuals. Nature *582*, 240–245. https://doi.org/10.1038/s41586-020-2263-3.
19. Suo, C., Yang, Y., Yuan, Z., Zhang, T., Yang, X., Qing, T., Gao, P., Shi, L., Fan, M., Cheng, H., et al. (2019). Alcohol Intake Interacts with Functional Genetic Polymorphisms of Aldehyde Dehydrogenase (ALDH2) and Alcohol Dehydrogenase (ADH) to Increase Esophageal Squamous Cell Cancer Risk. J. Thorac. Oncol. *14*, 712–725. https://doi.org/10.1016/j.jtho.2018.12.023.
20. Gao, Y., Zhou, Z., Ren, T., Kim, S.-J., He, Y., Seo, W., Guillot, A., Ding, Y., Wu, R., Shao, S., et al. (2019). Alcohol inhibits T-cell glucose metabolism and hepatitis in ALDH2-deficient mice and humans: roles of acetaldehyde and glucocorticoids. Gut *68*, 1311–1322. https://doi.org/10.1136/gutjnl-2018-316221.
21. Chang, Y.C., Lee, H.L., Yang, W., Hsieh, M.L., Liu, C.C., Lee, T.Y., Huang, J.Y., Nong, J.Y., Li, F.A., Chuang, H.L., et al. (2023). A common East-Asian ALDH2 mutation causes metabolic disorders and the therapeutic effect of ALDH2 activators. Nat. Commun. *14*, 5971. https://doi.org/10.1038/s41467-023-41570-6.
22. Seo, W., Gao, Y., He, Y., Sun, J., Xu, H., Feng, D., Park, S.H., Cho, Y.E., Guillot, A., Ren, T., et al. (2019). ALDH2 deficiency promotes alcohol-associated liver cancer by activating oncogenic pathways via oxidized DNA-enriched extracellular vesicles. J. Hepatol. *71*, 1000–1011. https://doi.org/10.1016/j.jhep.2019.06.018.
23. Perez-Miller, S., Younus, H., Vanam, R., Chen, C.H., Mochly-Rosen, D., and Hurley, T.D. (2010). Alda-1 is an agonist and chemical chaperone for the common human aldehyde dehydrogenase 2 variant. Nat. Struct. Mol. Biol. *17*, 159–164. https://doi.org/10.1038/nsmb.1737.
24. Yang, L., Roh, Y.S., Song, J., Zhang, B., Liu, C., Loomba, R., and Seki, E. (2014). Transforming growth factor beta signaling in hepatocytes participates in steatohepatitis through regulation of cell death and lipid metabolism in mice. Hepatology *59*, 483–495. https://doi.org/10.1002/hep.26698.
25. Vujovic, N., Piron, M.J., Qian, J., Chellappa, S.L., Nedeltcheva, A., Barr, D., Heng, S.W., Kerlin, K., Srivastav, S., Wang, W., et al. (2022). Late isocaloric eating increases hunger, decreases energy expenditure, and modifies metabolic pathways in adults with overweight and obesity. Cell Metabol. *34*, 1486–1498. https://doi.org/10.1016/j.cmet.2022.09.007.
26. Yadav, H., Quijano, C., Kamaraju, A.K., Gavrilova, O., Malek, R., Chen, W., Zerfas, P., Zhigang, D., Wright, E.C., Stuelten, C., et al. (2011). Protection from obesity and diabetes by blockade of TGF-beta/Smad3 signaling. Cell Metabol. *14*, 67–79. https://doi.org/10.1016/j.cmet.2011.04.013.
27. Zhao, J., Hu, L., Gui, W., Xiao, L., Wang, W., Xia, J., Fan, H., Li, Z., Zhu, Q., Hou, X., et al. (2022). Hepatocyte TGF-beta Signaling Inhibiting WAT Browning to Promote NAFLD and Obesity Is Associated With Let-7b-5p. Hepatol. Commun. *6*, 1301–1321. https://doi.org/10.1002/hep4.1892.
28. Pan, Q., Ai, W., Chen, Y., Kim, D.M., Shen, Z., Yang, W., Jiang, W., Sun, Y., Safe, S., and Guo, S. (2023). Reciprocal Regulation of Hepatic TGF-beta1 and Foxo1 Controls Gluconeogenesis and Energy Expenditure. Diabetes *72*, 1193–1206. https://doi.org/10.2337/db23-0180.
29. Walton, K.L., Johnson, K.E., and Harrison, C.A. (2017). Targeting TGF-beta Mediated SMAD Signaling for the Prevention of Fibrosis. Front. Pharmacol. *8*, 461. https://doi.org/10.3389/fphar.2017.00461.
30. Bellomo, C., Caja, L., and Moustakas, A. (2016). Transforming growth factor beta as regulator of cancer stemness and metastasis. Br. J. Cancer *115*, 761–769. https://doi.org/10.1038/bjc.2016.255.
31. Yu, L., Hébert, M.C., and Zhang, Y.E. (2002). TGF-beta receptor-activated p38 MAP kinase mediates Smad-independent TGF-beta responses. EMBO J. *21*, 3749–3759. https://doi.org/10.1093/emboj/cdf366.
32. Voelker, J., Berg, P.H., Sheetz, M., Duffin, K., Shen, T., Moser, B., Greene, T., Blumenthal, S.S., Rychlik, I., Yagil, Y., et al. (2017). Anti-TGF-beta1 Antibody Therapy in Patients with Diabetic Nephropathy. J. Am. Soc. Nephrol. *28*, 953–962. https://doi.org/10.1681/ASN.2015111230.
33. Petersen, M., Thorikay, M., Deckers, M., van Dinther, M., Grygielko, E.T., Gellibert, F., de Gouville, A.C., Huet, S., ten Dijke, P., and Laping, N.J. (2008). Oral administration of GW788388, an inhibitor of TGF-beta type I and II receptor kinases, decreases renal fibrosis. Kidney Int. *73*, 705–715. https://doi.org/10.1038/sj.ki.5002717.
34. Noble, P.W., Albera, C., Bradford, W.Z., Costabel, U., Glassberg, M.K., Kardatzke, D., King, T.E., Jr., Lancaster, L., Sahn, S.A., Szwarcberg, J., et al. (2011). Pirfenidone in patients with idiopathic pulmonary fibrosis (CAPACITY): two randomised trials. Lancet *377*, 1760–1769. https://doi.org/10.1016/s0140-6736(11)60405-4.
35. Liu, S., Ren, J., and Ten Dijke, P. (2021). Targeting TGFβ signal transduction for cancer therapy. Signal Transduct. Targeted Ther. *6*, 8. https://doi.org/10.1038/s41392-020-00436-9.
36. Yang, P., Yang, Y., Sun, P., Tian, Y., Gao, F., Wang, C., Zong, T., Li, M., Zhang, Y., Yu, T., and Jiang, Z. (2021). betaII spectrin (SPTBN1): biological function and clinical potential in cancer and other diseases. Int. J. Biol. Sci. *17*, 32–49. https://doi.org/10.7150/ijbs.52375.
37. Chen, J., Shukla, V., Farci, P., Andricovich, J., Jogunoori, W., Kwong, L.N., Katz, L.H., Shetty, K., Rashid, A., Su, X., et al. (2017). Loss of the transforming growth factor-beta effector beta2-Spectrin promotes genomic instability. Hepatology *65*, 678–693. https://doi.org/10.1002/hep.28927.
38. Tang, Y., Katuri, V., Dillner, A., Mishra, B., Deng, C.X., and Mishra, L. (2003). Disruption of transforming growth factor-beta signaling in ELF beta-spectrin-deficient mice. Science *299*, 574–577. https://doi.org/10.1126/science.1075994.
39. Tang, Y., Katuri, V., Srinivasan, R., Fogt, F., Redman, R., Anand, G., Said, A., Fishbein, T., Zasloff, M., Reddy, E.P., et al. (2005). Transforming growth factor-beta suppresses nonmetastatic colon cancer through Smad4 and adaptor protein ELF at an early stage of tumorigenesis. Cancer Res. *65*, 4228–4237. https://doi.org/10.1158/0008-5472.Can-04-4585.
40. Zhi, X., Lin, L., Yang, S., Bhuvaneshwar, K., Wang, H., Gusev, Y., Lee, M.H., Kallakury, B., Shivapurkar, N., Cahn, K., et al. (2015). betaII-Spectrin (SPTBN1) suppresses progression of hepatocellular carcinoma and Wnt signaling by regulation of Wnt inhibitor kallistatin. Hepatology *61*, 598–612. https://doi.org/10.1002/hep.27558.
41. Chen, J., Yao, Z.X., Chen, J.S., Gi, Y.J., Muñoz, N.M., Kundra, S., Herlong, H.F., Jeong, Y.S., Goltsov, A., Ohshiro, K., et al. (2016). TGF-β/β2-spectrin/CTCF-regulated tumor suppression in human stem cell disorder Beckwith-Wiedemann syndrome. J. Clin. Invest. *126*, 527–542. https://doi.org/10.1172/jci80937.
42. Korkut, A., Zaidi, S., Kanchi, R.S., Rao, S., Gough, N.R., Schultz, A., Li, X., Lorenzi, P.L., Berger, A.C., Robertson, G., et al. (2018). A Pan-Cancer Analysis Reveals High-Frequency Genetic Alterations in Mediators of Signaling by the TGF-beta Superfamily. Cell Syst. *7*, 422–437.e7. https://doi.org/10.1016/j.cels.2018.08.010.
43. Li, Y., Deng, D., Höfer, C.T., Kim, J., Heo, W.D., Xu, Q., Liu, X., and Zi, Z. (2023). Liebig's law of the minimum in the TGF-β/SMAD pathway. Preprint at bioRxiv. https://doi.org/10.1101/2023.07.10.548398.

44. Baek, H.J., Lee, Y.M., Kim, T.H., Kim, J.Y., Park, E.J., Iwabuchi, K., Mishra, L., and Kim, S.S. (2016). Caspase-3/7-mediated Cleavage of beta2-spectrin is Required for Acetaminophen-induced Liver Damage. Int. J. Biol. Sci. *12*, 172–183. https://doi.org/10.7150/ijbs.13420.

45. Rao, S., Yang, X., Ohshiro, K., Zaidi, S., Wang, Z., Shetty, K., Xiang, X., Hassan, M.I., Mohammad, T., Latham, P.S., et al. (2021). beta2-spectrin (SPTBN1) as a therapeutic target for diet-induced liver disease and preventing cancer development. Sci. Transl. Med. *13*, eabk2267. https://doi.org/10.1126/scitranslmed.abk2267.

46. Chen, J., Zaidi, S., Rao, S., Chen, J.S., Phan, L., Farci, P., Su, X., Shetty, K., White, J., Zamboni, F., et al. (2018). Analysis of Genomes and Transcriptomes of Hepatocellular Carcinomas Identifies Mutations and Gene Expression Changes in the Transforming Growth Factor-β Pathway. Gastroenterology *154*, 195–210. https://doi.org/10.1053/j.gastro.2017.09.007.

47. Xiang, X., Bhowmick, K., Shetty, K., Ohshiro, K., Yang, X., Wong, L.L., Yu, H., Latham, P.S., Satapathy, S.K., Brennan, C., et al. (2024). Mechanistically based blood proteomic markers in the TGF-β pathway stratify risk of hepatocellular cancer in patients with cirrhosis. Genes Cancer *15*, 1–14. https://doi.org/10.18632/genesandcancer.234.

48. Wang, Y., Nakajima, T., Gonzalez, F.J., and Tanaka, N. (2020). PPARs as Metabolic Regulators in the Liver: Lessons from Liver-Specific PPAR-Null Mice. Int. J. Mol. Sci. *21*, 2061. https://doi.org/10.3390/ijms21062061.

49. Davies, S.S., and Guo, L. (2014). Lipid peroxidation generates biologically active phospholipids including oxidatively N-modified phospholipids. Chem. Phys. Lipids *181*, 1–33. https://doi.org/10.1016/j.chemphyslip.2014.03.002.

50. Schwabe, R.F., Tabas, I., and Pajvani, U.B. (2020). Mechanisms of Fibrosis Development in Nonalcoholic Steatohepatitis. Gastroenterology *158*, 1913–1928. https://doi.org/10.1053/j.gastro.2019.11.311.

51. Schneider, C., Tallman, K.A., Porter, N.A., and Brash, A.R. (2001). Two distinct pathways of formation of 4-hydroxynonenal. Mechanisms of nonenzymatic transformation of the 9- and 13-hydroperoxides of linoleic acid to 4-hydroxyalkenals. J. Biol. Chem. *276*, 20831–20838. https://doi.org/10.1074/jbc.M101821200.

52. Matsuura, I., Denissova, N.G., Wang, G., He, D., Long, J., and Liu, F. (2004). Cyclin-dependent kinases regulate the antiproliferative function of Smads. Nature *430*, 226–231. https://doi.org/10.1038/nature02650.

53. Pang, Y., Gara, S.K., Achyut, B.R., Li, Z., Yan, H.H., Day, C.P., Weiss, J.M., Trinchieri, G., Morris, J.C., and Yang, L. (2013). TGF-beta signaling in myeloid cells is required for tumor metastasis. Cancer Discov. *3*, 936–951. https://doi.org/10.1158/2159-8290.CD-12-0527.

54. Chang, J.S., Hsiao, J.R., and Chen, C.H. (2017). ALDH2 polymorphism and alcohol-related cancers in Asians: a public health perspective. J. Biomed. Sci. *24*, 19. https://doi.org/10.1186/s12929-017-0327-y.

55. Chen, C.H., Ferreira, J.C.B., Joshi, A.U., Stevens, M.C., Li, S.J., Hsu, J.H.M., Maclean, R., Ferreira, N.D., Cervantes, P.R., Martinez, D.D., et al. (2020). Novel and prevalent non-East Asian ALDH2 variants; Implications for global susceptibility to aldehydes' toxicity. EBioMedicine *55*, 102753. https://doi.org/10.1016/j.ebiom.2020.102753.

56. Cousin, M.A., Creighton, B.A., Breau, K.A., Spillmann, R.C., Torti, E., Dontu, S., Tripathi, S., Ajit, D., Edwards, R.J., Afriyie, S., et al. (2021). Pathogenic SPTBN1 variants cause an autosomal dominant neurodevelopmental syndrome. Nat. Genet. *53*, 1006–1021. https://doi.org/10.1038/s41588-021-00886-z.

57. Cheng, H., Zhang, N., and Pati, D. (2020). Cohesin subunit RAD21: From biology to disease. Gene *758*, 144966. https://doi.org/10.1016/j.gene.2020.144966.

58. Kwon, Y.J., Kim, J.O., Park, J.M., Choi, J.E., Park, D.H., Song, Y., Kim, S.J., Lee, J.W., and Hong, K.W. (2020). Identification of Genetic Factors Underlying the Association between Sodium Intake Habits and Hypertension Risk. Nutrients *12*, 2580. https://doi.org/10.3390/nu12092580.

59. Oikonomou, D., Georgiopoulos, G., Katsi, V., Kourek, C., Tsioufis, C., Alexopoulou, A., Koutli, E., and Tousoulis, D. (2018). Non-alcoholic fatty liver disease and hypertension: coprevalent or correlated? Eur. J. Gastroenterol. Hepatol. *30*, 979–985. https://doi.org/10.1097/MEG.0000000000001191.

60. Yu, H.-S., Oyama, T., Isse, T., Kitakawa, K., Ogawa, M., Pham, T.-T.-P., and Kawamoto, T. (2009). Characteristics of aldehyde dehydrogenase 2 (Aldh2) knockout mice. Toxicol. Mech. Methods *19*, 535–540. https://doi.org/10.3109/15376510903401708.

61. Wang, Z., Budhu, A.S., Shen, Y., Wong, L.L., Hernandez, B.Y., Tiirikainen, M., Ma, X., Irwin, M.L., Lu, L., Zhao, H., et al. (2021). Genetic susceptibility to hepatocellular carcinoma in chromosome 22q13.31, findings of a genome-wide association study. JGH Open *5*, 1363–1372. https://doi.org/10.1002/jgh3.12682.

62. Boyle, A.P., Hong, E.L., Hariharan, M., Cheng, Y., Schaub, M.A., Kasowski, M., Karczewski, K.J., Park, J., Hitz, B.C., Weng, S., et al. (2012). Annotation of functional variation in personal genomes using RegulomeDB. Genome Res. *22*, 1790–1797. https://doi.org/10.1101/gr.137323.112.

63. Suda, T., Gao, X., Stolz, D.B., and Liu, D. (2007). Structural impact of hydrodynamic injection on mouse liver. Gene Ther. *14*, 129–137. https://doi.org/10.1038/sj.gt.3302865.

64. Hossain, Z., Valicherla, G.R., Gupta, A.P., Syed, A.A., Riyazuddin, M., Chandra, S., Siddiqi, M.I., and Gayen, J.R. (2018). Discovery of pancreastatin inhibitor PSTi8 for the treatment of insulin resistance and diabetes: studies in rodent models of diabetes mellitus. Sci. Rep. *8*, 8715. https://doi.org/10.1038/s41598-018-27018-8.

65. Sasser, T.A., Chapman, S.E., Li, S., Hudson, C., Orton, S.P., Diener, J.M., Gammon, S.T., Correcher, C., and Leevy, W.M. (2012). Segmentation and measurement of fat volumes in murine obesity models using X-ray computed tomography. J. Vis. Exp. e3680. https://doi.org/10.3791/3680.

66. Tan, P., Pepin, É., and Lavoie, J.L. (2018). Mouse Adipose Tissue Collection and Processing for RNA Analysis. J. Vis. Exp. 57026. https://doi.org/10.3791/57026.

67. Roy, D., Myers, J.M., and Tedeschi, A. (2022). Protocol for assessing ex vivo lipolysis of murine adipose tissue. STAR Protoc. *3*, 101518. https://doi.org/10.1016/j.xpro.2022.101518.

68. Kostrzewski, T., Maraver, P., Ouro-Gnao, L., Levi, A., Snow, S., Miedzik, A., Rombouts, K., and Hughes, D. (2020). A Microphysiological System for Studying Nonalcoholic Steatohepatitis. Hepatol. Commun. *4*, 77–91. https://doi.org/10.1002/hep4.1450.

69. Cheema, A.K., Pathak, R., Zandkarimi, F., Kaur, P., Alkhalil, L., Singh, R., Zhong, X., Ghosh, S., Aykin-Burns, N., and Hauer-Jensen, M. (2014). Liver metabolomics reveals increased oxidative stress and fibrogenic potential in gfrp transgenic mice in response to ionizing radiation. J. Proteome Res. *13*, 3065–3074. https://doi.org/10.1021/pr500278t.

70. Prince, J.T., and Marcotte, E.M. (2006). Chromatographic alignment of ESI-LC-MS proteomics data sets by ordered bijective interpolated warping. Anal. Chem. *78*, 6140–6152. https://doi.org/10.1021/ac0605344.

71. Libiseller, G., Dvorzak, M., Kleb, U., Gander, E., Eisenberg, T., Madeo, F., Neumann, S., Trausinger, G., Sinner, F., Pieber, T., and Magnes, C. (2015). IPO: a tool for automated optimization of XCMS parameters. BMC Bioinf. *16*, 118. https://doi.org/10.1186/s12859-015-0562-8.

72. Pang, Z., Chong, J., Zhou, G., de Lima Morais, D.A., Chang, L., Barrette, M., Gauthier, C., Jacques, P.É., Li, S., and Xia, J. (2021). MetaboAnalyst 5.0: narrowing the gap between raw spectra and functional insights. Nucleic Acids Res. *49*, W388–W396. https://doi.org/10.1093/nar/gkab382.

73. Fiser, A., and Sali, A. (2003). ModLoop: automated modeling of loops in protein structures. Bioinformatics *19*, 2500–2501. https://doi.org/10.1093/bioinformatics/btg362.

74. Guex, N., and Peitsch, M.C. (1997). SWISS-MODEL and the Swiss-PdbViewer: an environment for comparative protein modeling. Electrophoresis *18*, 2714–2723. https://doi.org/10.1002/elps.1150181505.

75. Morris, G.M., Huey, R., Lindstrom, W., Sanner, M.F., Belew, R.K., Goodsell, D.S., and Olson, A.J. (2009). AutoDock4 and AutoDockTools4: Automated docking with selective receptor flexibility. J. Comput. Chem. *30*, 2785–2791. https://doi.org/10.1002/jcc.21256.

76. Mohammad, T., Mathur, Y., and Hassan, M.I. (2021). InstaDock: A single-click graphical user interface for molecular docking-based virtual high-throughput screening. Briefings Bioinf. *22*, bbaa279. https://doi.org/10.1093/bib/bbaa279.

STAR★METHODS

KEY RESOURCES TABLE

REAGENT or RESOURCE	SOURCE	IDENTIFIER
Antibodies		
Anti-4-HNE	R&D Systems	Cat# MAB3249; RRID: AB_664165
Anti-ALDH2	Proteintech	Cat# 15310-1-AP; RRID: AB_2224185
Anti-VINCULIN	Sigma-Aldrich	Cat# V9131; RRID: AB_477629
Anti-SPTBN1	Chen et al.[41]	N/A
Anti-SMAD3	Cell Signaling	Cat# 9523; RRID:AB_2193182
Anti-pSMAD3	Cell Signaling	Cat# 9520; RRID:AB_2193207
Anti-V5	Invitrogen	Cat# R96025; RRID: AB_2556564
Anti-GAPDH	Cell Signaling	Cat# 97166; RRID: AB_2756824
Anti-Collagen type I	Rockland	Cat# 600-401-103; RRID: AB_2074625
Anti-αSMA	Abcam	Cat# Ab7817; RRID: AB_262054
Anti-AKT	Cell Signaling	Cat# 4691; RRID:AB_915783
Anti-pAKT	Cell Signaling	Cat#4060; RRID:AB_2315049
Normal mouse IgG	MilliporeSigma™	Cat# NI03100UG; RRID: AB_490557
Normal rabbit IgG	Cell Signaling	Cat# 2729; RRID: AB_1031062
Anti-rabbit IgG, HRP-linked Antibody	Cell Signaling	Cat# 7074P2; RRID: AB_2099233
Anti-mouse IgG, HRP-linked Antibody	Cell Signaling	Cat# 7076P2; RRID: AB_330924
Bacterial and virus strains		
DH5alpha Chemically Competent Cells (High Efficiency)	NEB	Cat# C2987H
Chemicals, peptides, and recombinant proteins		
4-hydroxynonenal (HNE)	Cayman	Cat# 32100
Insulin solution	Sigma-Aldrich	Cat# I0516-5ML
Glucose solution	Sigma-Aldrich	Cat# G8769-100ML
TRI Reagent™ Solution	Thermo Fisher Scientific	Cat# AM9738
PowerUp™ SYBR™ Green Master Mix	Applied Biosystem	Cat# A25742
Nitrocellulose Blotting Membrane	Bio-Rad	Cat# 1620112
Protein A/G Mix Magnetic Beads	MilliporeSigma	Cat# LSKMAGAG02
Lipofectamine™ RNAiMAX Transfection Reagent	Thermo Fisher Scientific	Cat# 13778075
Lipofectamine™ LTX Reagent with PLUS™ Reagent	Thermo Fisher Scientific	Cat# 15338100
PhosSTOP™ EASYpack	MilliporeSigma	Cat# 4906837001
cOmplete™, Mini, EDTA-free Protease Inhibitor Cocktail	MilliporeSigma	Cat# 11836170001
TransIT®-QR hydrodynamic delivery solution	Mirus	MIR 5240
DMEM/F12 medium	Corning	Cat# 10-090-CV
DMEM, high glucose	Thermo Fisher Scientific	Cat# 11965092
Critical commercial assays		
Aspartate Aminotransferase (AST) Activity Colorimetric Assay Kit	Biovision	Cat# K753
Alanine Aminotransferase (ALT) Activity Colorimetric Assay Kit	Biovision	Cat# K752
OxiSelect™ HNE Adduct Competitive ELISA Kit	Cell Biolabs	Cat# STA-838

(*Continued on next page*)

Continued

REAGENT or RESOURCE	SOURCE	IDENTIFIER
Insulin Mouse ELISA Kit	Thermo Fisher Scientific	Cat# EMINS
Free Fatty Acid Quantitation Kit	Sigma-Aldrich	Cat# MAK044
Glycerol Assay Kit	abcam	Cat# ab133130
TaqMan™ Reverse Transcription Kit	Applied Biosystem	Cat# 43-665-96
VECTASTAIN® Elite ABC-HRP Kit, Peroxidase	Vector Laboratories	Cat# PK-6106
EnVision®+ Dual Link System-HRP (DAB+)	Agilent Technologies	Cat# K4065
RNeasy Plus Mini kit	Qiagen	Cat# 74134
Deposited data		
Metabolomics and lipidomics data	National Metabolomics Data Repository (NMDR)	Metabolomics Workbench Accession #: PR002095, https://www.metabolomicsworkbench.org/data/DRCCMetadata.php?Mode=Project&ProjectID=PR002095. DOI:https://doi.org/10.21228/M8TC1H
Mass spectrometry data	ProteomeXchange Consortium	PXD055145
Source data	Mendeley data	Mendeley: 10.17632/nrpm8ydybr.1
RNA-sequencing data	GEO	GSE273561
Experimental models: Cell lines		
Huh7	ATCC	Cat# HB-8065
HepG2	ATCC	Cat# PTA-4583
LX-2 Human Hepatic Stellate Cell Line	Sigma-Aldrich	Cat# SCC064
Experimental models: Organisms/strains		
Mouse: *Sptbn1*$^{+/-}$:129SvEv X Black Swiss	Chen et al.[41]	
Mouse: *Aldh2*$^{-/-}$: C57BL/6J	Dr. Agata Smogorzewska	
Oligonucleotides		
Ambion *in vivo* pre-designed siRNA siRNA ID: s74306	Thermo Fisher Scientific	Cat# 4457302
Silencer™ Cy™3-labeled Negative Control No. 1 siRNA	Thermo Fisher Scientific	Cat# AM4621
Ambion Silencer® Negative Control# 1 siRNA	Thermo Fisher Scientific	Cat# AM4611
ON-TARGETplus Mouse SPTBN1 siRNA	Horizon Discovery	Cat# L-043666-01-0005
ON-TARGETplus Human SPTBN1 siRNA	Horizon Discovery	Cat# L-018149-01-0005
ON-TARGETplus Non-targeting Control Pool	Horizon Discovery	Cat# D-001810-10-05
qPCR primers used in this study	Table S5	N/A
Recombinant DNA		
Plasmid: pcDNA3.1/V5-mouse SPTBN1 full length	Rao et al.[45]	
Plasmid: pcDNA3.1/V5-mouse NSPTBN1 (1-1455)	Rao et al.[45]	
Plasmid: pcDNA3.1/V5-mouse CSPTBN1	Rao et al.[45]	
Plasmid: human pCMV3- ALDH2-FLAG	Sino Biological	Cat# HG12064-CF
Software and algorithms		
R 4.2	R software foundation	https://www.r-project.org/
DESeq2 (version 1.18.1)		https://bioconductor.org/packages/release/bioc/html/DESeq2.html
GraphPad Prism	GraphPad Sofware INC	https://www.graphpad.com/scientific-software/prism/
Other		
Synergy H1 hybrid reader	BioTek	
CardioChek PA analyzer	Pts Diagnostics	
AimStrip® Plus Blood Glucose Meter	Germaine Laboratories	
NanoDrop 2000 Spectrophotometer	Thermo Fisher Scientific	Cat# ND-2000
CFX96 Real-Time PCR system	Bio-Rad	

(*Continued on next page*)

Continued

REAGENT or RESOURCE	SOURCE	IDENTIFIER
Trans-Blot Turbo transfer system	Bio-Rad	Cat# 1704150J2
Eclipse E800 microscope	Nikon	
MMC100 metabolic cage	Hatteras instruments	

EXPERIMENTAL MODEL AND STUDY PARTICIPANT DETAILS

Husbandry, diets, and dietary intervention in mice

All animal experiments were performed according to the guidelines for the care and use of laboratory animals and were approved by the Institutional Biomedical Research Ethics Committee of The George Washington University for Biomedical Research. *Aldh2*$^{-/-}$ mice on C57BL/6J background obtained from Dr. Agata Smogorzewska at Rockefeller University were intercrossed with *Sptbn1*$^{+/-}$ mice on a 129SvEv × Black Swiss to generate double mutant *Aldh2*$^{-/-}$ *Sptbn1*$^{+/-}$ (ASKO). *Sptbn1*^{LSKO} mice were generated as previously described.[45] *Aldh2*$^{-/-}$ mice intercrossed with *Sptbn1*^{LSKO} mice to generate *Aldh2*$^{-/-}$*Sptbn1*^{LSKO} mice. All mice were housed under a standard light cycle (12 h light: 12 h dark) at 23–25°C and humidity (~50%).

For the Western diet (WD) induced liver steatosis and MASH model, 10-week-old male and female *Aldh2*$^{-/-}$ mice or *Aldh2*$^{-/-}$ *Sptbn1*^{LSKO} mice were fed a diet containing 42% kcal from fat (TD.88137) together with a high fructose-glucose solution (SW: 23.1 g/L D-fructose+18.9 g/L D-glucose) for 12 weeks. For DEN plus WDinduced MASH associated HCC, single dose of DEN (25 mg/kg) was injected in 14–15-day old male and female mice. WD was started 8 weeks after the DEN injection and animals received WD for a total of 10 months.

Patient samples for single-nucleotide polymorphism analysis

Patients with or without fatty liver diseases or high body mass index (BMI ≥30) (Tables S1 and S2) were from two case-control studies, the Yale Liver Health Study (YLHS) and the National Cancer Institute/University of Maryland School of Medicine (NCI-UMD) study.[61] Both studies were approved by IRBs at all participating institutions and organizations. All patients provided informed consent for the use of clinical or omics data and samples for research purposes.[61]

METHOD DETAILS

Cell lines

Human liver cancer cell lines, HepG2 and Huh7, were purchased from American Type Culture Collection (ATCC). All cells were cultured in a complete culture medium, DMEM/F12 medium supplemented with 1% Streptomycin-Penicillin and 10% fetal bovine serum (FBS). Human Hepatic Stellate Cell Line, LX-2, was purchased from Sigma-Aldrich. LX-2 cells were cultured DMEM high glucose medium supplemented with 1% Streptomycin-Penicillin and 2% fetal bovine serum.

Single-nucleotide polymorphism determination and statistical analysis for association with obesity or liver disease

The "fatty liver diseases" group included patients with MASLD or MASH. Demographic data for the patients in the health groups were presented as numbers with percentages for categorical variables and as mean with standard deviation for continuous variables. Wilcoxon rank-sum test was used for comparison of continuous variables. The chi-square test or Fisher exact test was used for categorical variables as appropriate. All statistical tests were two-sided, comparisons were made between two groups (fatty liver diseases vs. control or high BMI ≥30 vs. low BMI <25). SNPs were defined using GRCh37/hg19 as the reference genome. Associations between SNPs in *SPTBN1* or *ALDH2* and different health groups were based on an additive logistic regression model with adjustment for age, sex, and race using PLINK 2.0 (http://www.cog-genomics.org/plink/2.0). Among the 52 SNPs identified, any SNP with a *p* value less than 0.05 was included. Among the 22 SNPs meeting the 0.05 threshold, significant associations with the high BMI or fatty liver disease were defined using an adjusted *p* value less than 0.00096154 (0.05/52). Odds ratios (ORs) and 95% confidence intervals were calculated using the additive logistic regression model. Expression quantitative trait loci (eQTL) analysis of the SNPs was performed with GTEx V8 (https://www.gtexportal.org/home/), and chromatin- or DNA-binding proteins for SNPs were assessed with RegulomeDB (https://regulomedb.org/regulome-search/).[62]

Hydrodynamic *in vivo* siRNA targeting

For *in vivo* hydrodynamic siRNA injection, siRNA targeting mouse *Sptbn1* or control siRNA were resuspended in nuclease-free water and incubated with Lipofectamine RNAiMAX at a 1:1 ratio at room temperature. These complexes were diluted with TransIT-QR hydrodynamic delivery solution. Mice received 2.0 mL of diluted siRNA solution through hydrodynamic tail vein injection as previously described.[45,63] The injection was repeated 4 times in 7 weeks with 2 week intervals between injections. Mice were sacrificed on the same day of the last siRNA injection.

Measurements of serum triglycerides (TGs), glucose, insulin, and liver enzyme (ALT)

Terminal collection of blood was done through cardiac puncture to obtain maximum amount of blood. Blood glucose was measured by the glucose meter (Germaine Laboratories). Blood TG was measured by CardioChek PA analyzer (PTS Diagnostics) using PTS lipid panel test strips (PTS Diagnostics, #1710). Serum insulin levels were measured by ELISA (Thermo Fisher Scientific, #EMINS). Serum ALT values were measured by enzymatic colorimetric assays (Biovision, #K752).

Glucose tolerance test (GTT) and insulin tolerance test (ITT)

Mice were weighed on the day of the GTT procedure following overnight fast. Before glucose injection, a blood sample (~10 μL) was obtained from the tail vein to measure fasting blood glucose using a glucose meter (Germaine Laboratories). Glucose (2 g/kg body weight) was injected intraperitoneally, and glucose concentrations were measured at 30, 60, 90, and 120 min. For ITT, blood glucose was measured in mice fasted for 6 h before insulin injection to obtain basal glucose levels. Insulin (1 IU/kg) (Sigma-Aldrich) was injected intraperitoneally, and glucose concentrations were measured at 30, 60, 90, and 120 min[64]

Immunoblotting and co-immunoprecipitation (IP) analyses

Cells were lysed with freshly prepared RIPA buffer (20 mM Tris-HCl pH7.4, 150 mM NaCl, 1 mM EDTA, 1% Triton X-100, 1% sodium deoxycholate, 0.1% SDS) or NP-40 lysis buffer (50 mM Tris-HCl, pH 7.5, 0.15 M NaCl, 1% NP-40, 1 mM EDTA) with complete protease inhibitor and phosphatase inhibitor cocktails (MilliporeSigma), followed by SDS-PAGE and immunoblotting using different antibodies. For co-IP, whole cell lysate was precleared with protein A/G magnetic beads for 30 min to prevent non-specific binding of cellular proteins, followed by IP for overnight using protein A/G magnetic beads mixed with anti-SPTBN1[41] (rabbit IgG as the control) or anti-V5 (mouse IgG as the control). Immunoprecipitated complexes (magnetic bead-lysate-antibody mixtures) were washed 3–4 times with wash buffer (10 mM EDTA-Tris, 150 mM NaCl, 20 mM $MgCl_2$) and eluted with sample buffer followed by SDS-PAGE and immunoblotting analysis with anti-4-HNE (R&D Systems), anti-V5 (Invitrogen), anti-SPTBN1,[41] or anti-VINCULIN (Sigma-Aldrich).

CT scan

To assess the volume of body fat and lean tissue, mice were scanned by microCT.[65] Anesthesia was induced with 3% isoflurane in oxygen and maintained at 2% isoflurane. Whole-body CT was acquired on a Mediso nanoScan PET/CT (Mediso USA, Arlington, VA, USA), calibrated to Hounsfield Units. 720 projections were acquired at 50 kVp energy and 189 μm. As exposure, and images were reconstructed in Nucline software (Mediso USA) using a filtered back-projection algorithm with a Blackman filter to a voxel size of 188 μm isotropic.

CT images were analyzed in VivoQuant 2021 (Invicro, Needham, MA, USA) using a custom script (available upon request). Briefly, after removing the imaging cradle from the CT image, a lower threshold of −500 HU was applied to segment the whole mouse and calculate its volume. Next, the lungs were segmented and combined with an automatically-thresholded airspace region of interest. This region of interest (ROI) was dilated to cover regions between dense tissue and airspace, which would otherwise be falsely counted as less-dense fat. Finally, a threshold between −400 and −100 HU was applied to the whole-body image, not including the dilated airspace ROI, to segment fat, and a threshold between −100 and 300 HU was applied to the whole-body image, excluding the airspace and urinary bladder, to segment lean tissue. The volumes of these fat and lean ROI's were then divided by the whole-body volume to calculate the percent fat and lean tissue values.[65]

Measurements of liver, visceral fat, and tissue histology

The whole liver, and both sides of perigonadal visceral adipose tissues[66] were excised and weighed. For liver tissue histology, liver tissues were fixed in 10% formalin. Routine tissue processing, including embedding in paraffin, sectioning, Hematoxylin and Eosin (H&E) staining, and Sirius red staining were done by the George Washington University histology facility core. Frozen liver tissues sections were stained with Oil Red O by VitroVivo biotech. For immunohistochemical analyses, FFPE liver tissue sections were probed with antibodies against anti-4-HNE (R&D Systems). Diaminobenzidine was used as a chromogen. Biotinylated secondary antibodies and the DAB kit were used for signal amplification and detection. Images were acquired with an Eclipse E800 microscope (Nikon) equipped with a Dxm1200F camera.

Measurement of *ex vivo* lipolysis

The *ex vivo* lipolysis assay has been performed as previously published protocol.[67] Briefly, about 50 mg eWAT and iWAT were treated by agonist (isoproterenol 10 μM) for 2 h in KRBH buffer (2% BSA) at 37°C. Collect media at 5 min and after 2 h. Then analysis fatty acids and glycerol by Free Fatty Acid Quantitation Kit (Sigma-Aldrich, MAK044) and Glycerol Assay Kit (Abcam, ab133130). Fatty acid and glycerol concentrations were normalized to tissue weight.

Measurements of food intake, water intake, and urine output

Mice fed a normal chow diet were housed individually in an MMC100 metabolic cage (Hatteras Instruments) for 24 h. Food intake was measured by differences in remaining food weight and water intake was measured by differences in remaining water volume before and after 24 h in the metabolic cage. The amount of urine produced in 24 h was measured by volume.

Immunofluorescence analyses

Huh7 or LX-2 cells were grown on cover glass transfected with siControl, siSptbn1, or siAldh2. Twelve hours post-transfection, cells were subjected to overnight starvation. Following day, cells were treated with 20 μM HNE for 4 h, followed by TGF-β (200 pM) treatment for 1 h. Cells were fixed using 4% paraformaldehyde for 15 min, PBS-washed, permeabilized in 0.5% Triton X-100 for 30 min and blocked in 1% bovine serum albumin in PBS for 30 min. Immunofluorescent staining was performed to detect SPTBN1 and SMAD3. Confocal images were acquired using a 20× objective on a Zeiss LSM880 confocal microscope.

Multiplex immunofluorescence staining

FFPE of mouse liver tissue were used to stain CD4, FoxP3, CD11b and F4/80. Optimal concentrations for each antibody were determined and using the optimized fluorophore. Stained tissue was counterstained and coverslipped with Antifade Mountant with NucBlue. Whole-slide imaging was performed on the Akoya Vectra Polaris machine. Images were processed by PhenoImager software. Multiplex immunofluorescence staining process was performed by HistoWiz, Inc. (Brooklyn, NY, USA).

Human 3D MASH culture and analysis

Human 3D MASH culture experiments were performed by CN Bio Innovations (United Kingdom).[68] Briefly, primary human hepatocytes, human Kupffer cells, and human stellate cells were seeded onto CN-Bio's PhysioMimix LC12 MPS culture plates at 6×10^5 cells for primary hepatocytes and 6×10^4 cells each for Kupffer cells and stellate cells (hepatocyte: Kupffer cell: stellate cell ratio = 10:1:1). MASH-inducing medium was added one day after the cells were plated, enabling the cells to form microtissues in the scaffold pores and initiating induction of a MASH phenotype. Four days after plating, fresh MASH-inducing medium was added, and cells were transfected with either 25 nM or 50 nM siRNA targeting *SPTBN1* or 25 nM of a control siRNA. On day 6 after plating, fresh MASH-inducing medium was added, and siRNA was replenished. Eight days after plating, cellular samples were evaluated for transcriptional profiling by RNA-seq, and cultures were processed for collagen type-I (Rockland) and α-SMA (Abcam) staining, and Hoechst was used to detect nuclei. Stained cultures were visualized by confocal microscopy. Mean intensities of collagen type-I staining, α-SMA staining, and Hoechst staining were measured in images acquired with the 10× objective across 9 fields of view from 8 slices of the scaffold. Each pore of the scaffold was treated as an individual data point. A total of 112–168 pores were measured. The intensity for α-SMA and Collagen Type-1 were normalized to Hoechst intensity to account for seeding density within each pore.

RNA extraction, RNA sequencing, and pathway analysis

For RNA-seq, RNA was extracted from liver tissues using the RNeasy Plus Mini kit. RNA quality and concentration were assessed using the Thermo Scientific Nanodrop spectrophotometer before RNA sequencing. About 1 μg of RNA was used to generate barcoded sequencing libraries. Novogene Corporation performed library preparation. RNA sequencing data was aligned using hisat2 V2.1.0 2 to the *Mus musculus* (GRCm38/mm10); the genes that passed the quality check were counted using HTSeq2 (v 0.11.1). The raw gene-level counts were then used for differential gene expression analysis using DESeq2. Gene expression was normalized using Log_2-transformed copies per million (Log_2CPM), and statistical significance ($p < 0.05$) was assessed by R using the Wald Test in DESeq2. Differentially expressed genes within groups were studied using Ingenuity Pathway Analysis (IPA, Qiagen) imputing the whole transcriptome and filtering it in IPA for statistically significant ($p < 0.05$) results with a log2 fold change (Log2FC) less than −0.3785 or greater than 0.3785, and FPKM >1 for mice. "Upstream Regulators" networks were generated and ranked in terms of the significance of participating genes and activation status (*Z* score). Biologically relevant results met the following criteria as previously described[45]: genes assigned to a regulatory network with a false discovery rate (FDR) < 0.05, statistical significance ($p < 0.05$) of the *Z* score >2 or *Z* score <−2 of the upstream regulator, and enrichment in 'significantly modulated' networks in the comparative analysis.

Metabolomic and lipidomic analyses

Polar metabolites and lipids were extracted from liver tissues with a mixture of acetonitrile and methanol and analyzed using an Acquity UPLC system online with electrospray quadrupole-time-of-flight tandem mass spectrometer (ESI-Q-TOF) (QTOF Premiere, Waters Corp, Milford, MA) as previously described.[69] Chromatographic separation was achieved on a 50 mm × 2.1 mm Acquity 1.7 μm C18 column using a flow rate of 0.5 mL/min with a capillary voltage of 3.2 kV and a sampling cone voltage of 35.0 V in positive mode. Operating conditions were 2.7 V extraction cone voltage; 120°C source temperature; 350°C desolvation temperature with 800 L/h desolvation gas flow rate; and 25 L/h cone gas flow rate. Mass spectra were obtained over the mass range of 50–1200 *m/z* in centroid mode. Sulfadimethoxine (500 pg/μL) in 50% acetonitrile ($[M + H]^+$, *m/z* 311.0814) was infused at 0.08 μL/min flow rate and served as the reference mass as previously described.[69]

For analysis of untargeted metabolomics and lipidomics data, raw MS data files were converted to NetCDF format using Databridge. NetCDF files were processed using an in-house implementation of the XCMS (Scripps Institute, La Jolla, CA) R package. XCMS was used for peak detection and retention time correction. Initially, the ion peaks were filtered and detected using the matched filter algorithm. The peak detection algorithm allows data to be binned into parts with predefined widths and mass, and it is then compared to known peaks of similar distributions. Retention time correction was performed using the Ordered Bijective Interpolated Warping (OBI-Warp) algorithm.[70] All parameters for the matched filter and OBI-Warp algorithm were optimized with the IPO

(Isotopologue Parameter Optimization) R package.[71] XCMS output produces *m/z* values, retention times, and ion intensities. Data were then normalized to the intensities of internal standards. Tissue data were also normalized to total protein concentration. Multivariate statistical analyses were then performed using Metaboanalyst[72] implemented in R, with log transformation and Pareto scaling.

Structure modeling and molecular docking simulations with SPTBN1 and 4-HNE

Molecular docking simulations were performed, and binding affinities for 4-HNE and SPTBN1 were calculated. Three-dimensional structural coordinates of SPTBN1 were obtained from the AlphaFold database (accession ID: Q01082). Due to the lack of structural folds, the SPTBN1 was modeled in three fragments covering D50-T975, Q1132-T2155, and A2198-K2364. Loop remodeling was performed using ModLoop.[73] All structures were energy minimized in Swiss-PDB Viewer[74] and refined further using the MGL AutoDock tools.[75] The 4-HNE structure was retrieved from the PubChem database in processed format (PubChem CID: 5283344). The docking simulations were performed using InstaDock[76] with a blind search space in which 4-HNE was free to move and search its favorable binding site(s) on SPTBN1. The grid box size for SPTBN1 (D50-T975) was set to (306 Å × 125 Å × 280 Å) and centralized at (−0.397, −0.310, −15.534) for the blind search space. The grid box size for SPTBN1 (Q1132-T2155) was set to (226 Å × 122 Å × 299 Å), centralized at (−7.560, −1.795, 1.034). The grid box size for SPTBN1 (A2198-K2364) was set to (275 Å × 134 Å × 252 Å), centralized at (−12.453, −1.867, 5.293). After estimating the binding affinity, all possible docked conformations of 4-HNE were split to further analyze their binding pattern with SPTBN1 using PyMOL and Discovery Studio Visualizer.

Quantification of free 4-HNE by mass spectrometry

Each liver tissue was weighed into an microcentrifuge tube. Acetonitrile (70%) containing 0.5 μg/mL of 4-HNE-d3 at 9 μL per mg raw tissue was added. The samples were homogenized with the aid of two metal beads on an MM 400 mill mixer at 30 Hz for 1 min, four times, followed by centrifugal clarification in a microfuge at 5°C for 15 min, and supernatants were collected. Standard solutions of 4-HNE were prepared in ethanol at a concentration range of 0.00005–1 μg/mL. The supernatant (100 μL metabolite extract) of each sample or each standard solution was mixed with 100 μL of a cyclohexanedione buffer solution. The mixtures were incubated at 50°C for 120 min. After the reaction, 10 μL aliquots of the mixtures were injected and analyzed by UPLC-MRM/MS on an Agilent 1290 UHPLC system coupled to an Agilent 6495B QQQ mass spectrometer operated in the positive-ion detection mode and using a C18 column (2.1 × 150 mm, 1.8 μm) and a mobile phase composed of 0.1% formic acid and acetonitrile for LC separation. The binary-solvent elution gradient was 20%–50% in 10 min at 0.35 mL/min and 50°C. Concentrations of 4-HNE in the samples were calculated by interpolating the constructed linear-regression, internal standard calibration curves with the analyte to internal standard peak area ratios measured from the sample solutions. The mass spectrometry proteomics data have been deposited to the ProteomeXchange Consortium via the PRIDE (https://www.ebi.ac.uk/pride/) partner repository with the dataset identifier PXD055145. We used 4-HNE-protein adduct ELISA (Cell Biolabs) to detect 4-HNE bound to proteins in mouse liver tissues according to the manufacturer's instructions.

snRNA-seq

Nuclei were isolated by lysing frozen mouse livers with a pestle and cold lysing buffer (10 mM Tris-HCl, pH 7.4, 10 mM NaCl, 3 mM $MgCl_2$, 0.1% NP-40, 0.4 U/μL RNase Inhibitor, 1mM DTT) for 4 min on ice. The lysate was filtered over a 40 μm filter, centrifuged at 500 g at 4 °C and resuspended in 1X PBS with 1% BSA & 0.4 U/μL RNase Inhibitor. Nuclei were labeled with 7-AAD (Sigma) and sorted on a BD FACS Aria to purify nuclei from the remaining debris. Sorted nuclei were counted and loaded onto a Chip G and 10X Genomics Chromium Controller to generate GEMs following the manufacturer's protocol (Chromium Next GEM Single Cell 3′ v3.1 with Dual Indexing). Libraries were quantitated and fragment sizes determined using a High Sensitivity DNA Chip and Bioanalyzer (Agilent). Sequencing was done at Medgenome (Foster City, CA) on a Novaseq at a depth of 50,000 reads per nuclei.

Quantitative PCR

Total RNA was extracted with the use of TRIzol reagent (Ambion) according to the manufacturer's instructions. Reverse transcription of total RNA to cDNA was performed according to the manufacturer's instructions. Each cDNA was amplified with the SYBR Green Master Mix. Primers for the real-time PCR are listed in key resources table for human (h) and mouse (m) genes.

QUANTIFICATION AND STATISTICAL ANALYSIS

For multiple comparisons, one-way ANOVA with post-hoc Bonferroni's test was used. Differences between 2 groups were evaluated using 2-tailed Student's t-tests using GraphPad Prism. *In vitro* experiments were performed 2–4 times. Results are presented as mean ± SEM unless otherwise indicated. For all statistical analyses, $p < 0.05$ was considered statistically significant.

For bioinformatics analysis to evaluate the relative mRNA abundance of *SPTBN1* and *ALDH2* in liver tissue samples from healthy obese individuals, patients with simple steatosis, or patients with MASH from the public datasets (GSE48452 and GSE89632), these datasets were processed using the interactive web tool GEO2R. Then, differences in gene expression among groups were analyzed with GraphPad Prism using one-way analysis of variance (ANOVA) with posthoc Bonferroni's test.